



Universität Hamburg
DER FORSCHUNG | DER LEHRE | DER BILDUNG

MASTERTHESIS

The Impact of Wind Drift on Radar-Derived Rainfall Estimates

Gregor Möller

supervised by

Dr. Marco Clemens
Prof. Dr. Felix Ament

METEOROLOGICAL INSTITUTE
UNIVERSITY OF HAMBURG

Hamburg, December 10, 2018

Topic:

The impact of wind drift on radar-derived rainfall estimates

Abstract

Operational weather radars measure at considerable height above the ground, depending on the distance to the radar site. To obtain useful information about precipitation at ground level effects such as wind drift must be taken into account. Two methods to determine the impact of wind drift on radar measurements are presented. Both methods are applied to six heavy precipitation events in June, 2016. The data is based on the volume scan of the polarimetric Doppler radar in Boostedt of the Deutscher Wetterdienst. The first method applies a template matching algorithm to find the shift between precipitation fields at different heights. This is a relative drift between different heights at a specific time. To find the relative drift to the ground, a profile of relative drift between several heights is extrapolated to the ground. These relative drift profiles show only little deviation to a linear fit with a mean RMSE of 120 m in drift distance and 2° in drift direction. They are also stable with a mean standard deviation of 153 m and 8° for all relative drift profiles from 30 minutes before until 30 minutes after the maximum of the precipitation event. The absolute wind drift that a precipitation field experiences while falling is found by adding the traveled distance of the original precipitation field to the relative drift at a specific time stamp. This procedure calculates absolute wind drift values of 3.8 km on average, ranging from 1 km to 7.9 km. For comparison, a second method to quantify the impact of wind drift is introduced: A simple advection scheme that simulates the drop size dependent trajectory of water droplets under the effect of wind drift. 10 drop bins from 0.5 mm to 5 mm are included. All droplet interactions are ignored. Only terminal velocity and wind-driven horizontal advection are considered. Simulations in stationary environments for artificially created precipitation fields are shown to illustrate the basic model characteristics. Initialized with sounding wind profiles, the advection scheme is then applied to non-stationary and radar measured precipitation fields, where wind drift values of 7.2 km are found on average, ranging from 2.1 km and 13.8 km.

Contents

1. Introduction	1
2. Data	5
2.1. Volumetric Radar Data	5
2.2. Six Precipitation Events	8
3. Analysis of Volumetric Radar Data	13
3.1. Precipitation Matching Algorithm	13
3.1.1. Coordinate Transformation	15
3.1.2. Interpolation	16
3.1.3. Template Matching	21
3.1.4. Profiles of Relative Drift	23
3.1.5. Calculation of Absolute Wind Drift	25
3.2. Application of the Precipitation Matching Algorithm	31
3.2.1. Resulting Relative Drift	31
3.2.2. Resulting Absolute Wind Drift	34
3.2.3. Stability of the Relative Drift Profiles	36
3.2.4. Correction of Precipitation Scans	37
4. A Simple Advection Scheme	43
4.1. Model Characteristics	43
4.2. Combination with PMA	54
5. Conclusion and Outlook	63
A. Plots for all Precipitation Events	73

List of Symbols

α	Radar azimuth angle
\bar{T}_v	Mean virtual temperature
$\delta(h)$	Height factor (eq. (3.21))
Δt	Length of time step (s)
γ	Normalized cross-correlation (eq. (3.11))
Λ	Slope of Marshall-Palmer distribution (eq. (3.17))
k_e	Refractivity factor (4/3)
N_0	Intercept of Marshall-Palmer distribution ($8 \cdot 10^3 \text{ mm}^{-1} \text{ m}^{-3}$)
R_d	Gas constant for dry air ($287 \text{ J K}^{-1} \text{ kg}^{-1}$)
ρ_w	Water density (10^3 kg m^{-3})
θ	Radar elevation angle
\vec{d}_r	Relative wind drift
\vec{d}_w	Absolute wind drift (eq. (3.12))
\vec{s}	Horizontal shift between CAPPs
\vec{v}	Horizontal wind vector
\vec{v}_h	Precipitation travel speed (eq. (3.14))
\vec{x}_t	Precipitation travel distance (eq. (3.13))
D	Drop diameter in mm
$d_{f,t}^2$	Squared Euclidean distance (eq. (3.10))
D_0	Median volume diameter (eq. (3.15))
h	Height above ground
h_1^2	Layer thickness (eq. (4.9))
j	Barycentric Coordinate j (eq. (3.5))
k	Barycentric Coordinate k (eq. (3.6))
l	Barycentric Coordinate l (eq. (3.7))

M	Total liquid water content (kg)
$N(D)$	Number of water drops at diameter D (eq. (3.16))
R	Rainfall Rate (mm h^{-1})
r	Radar range gate
s_h	Simulated horizontal displacement (eq. (4.3))
s_{arc}	Great-circle distance (eq. (3.1))
$t_f(h)$	Precipitation fall time (eq. (3.22))
$v_t(h)$	Terminal velocity (eq. (3.20))
x	Cartesian x-distance (eq. (3.3))
y	Cartesian y-distance (eq. (3.4))
Z	Relative reflectivity factor (eq. (3.9))
z	Reflectivity factor (eq. (4.6))
a	Earth's radius (6 370 m)
CAPPI	Constant Altitude Plan Position Indicator
CFL	Courant-Friedrichs-Lewy (eq. (4.4))
dBZ	Units of the relative reflectivity factor (eq. (3.9))
DWD	Deutscher Wetterdienst (German Meteorological Service)
g	Gravitiy acceleration (9.81 m s^{-2})
PMA	Precipitation Matching Algorithm
POLARA	Polarimetric Radar Algorithms
PPI	Plan Position Indicator
RMSE	Root mean square error
TM	Transverse Mercator

List of Figures

2.1. Radar network	6
2.2. Radar setup	7
2.3. Radar scan strategy	7
2.4. Original data	9
2.5. Precipitation scans	11
2.6. Soundings	12
3.1. Barycentric Coordinates	17
3.2. Interpolated reflectivity	20
3.3. Constant Altitude Plan Position Indicator	20
3.4. Correlation matrices	24
3.5. Relative drift profile	26
3.6. Difference between absolute and relative drift	28
3.7. Relative drift profiles c) and e) with offset	32
3.8. Stability of relative drift profile of event a)	38
3.9. Corrected radar scan of event c)	39
3.10. Reflectivity difference of event c)	40
3.11. Wind direction profile of event c)	41
4.1. Implementation of horizontal and vertical displacement	45
4.2. Displacement of grid volumes	47
4.3. Artificial precipitation field	49
4.4. Stationary simulation with artificial initialization	51
4.5. Non-stationary simulation with radar initialization	53
4.6. Wind speed profile obtained through PMA drift	56

4.7. Sounding wind profile	57
4.8. Non-stationary simulation with sounding wind profile	59
4.9. Simulated relative drift profile	60
A.1. Relative drift profiles a) to c)	74
A.2. Relative drift profiles d) to f)	75
A.3. Stability of relative drift profiles a) to c)	76
A.4. Stability of relative drift profiles d) to f)	77
A.5. Correlation matrices of all precipitation events	78
A.6. All corrected precipitation scans	79
A.7. Reflectivity difference of all events	80
A.8. Sounding wind profiles a) to c)	81
A.9. Sounding wind profiles d) to f)	82
A.10. Simulated relative drift profiles a) to c)	83
A.11. Simulated relative drift profiles d) to f)	84

List of Tables

2.1. Scan strategy	8
2.2. Precipitation events overview	10
3.1. RMSE of relative drift profiles	33
3.2. Relative and absolute drift of all events	35
3.3. Median volume diameter and travel speed	35
3.4. Standard deviation of relative drift profiles	37
4.1. Simulated wind drift values of all events	61
4.2. Simulated wind drift values without small droplets	61

Chapter 1

Introduction

Operational weather radar networks aim at producing accurate measurements of the spatial distribution of precipitation. This is important for many meteorological applications, such as numerical weather prediction, severe weather warnings or quantitative precipitation estimation. The measurement height of a radar beam increases with distance to the radar site due to the earth's curvature and the beam's elevation angle. At the same time, most applications are most (or only) interested in precipitation at ground level. It is known for a long time that the estimation of radar-derived rainfall at ground level is prone to many errors. These errors are linked for example to variations in drop size distributions, to the variability of vertical profiles of reflectivity, to the spatial variation of coalescence, partitioning or evaporation, to the enhancement of radar reflectivity by hailstones or melting snow (Bright Band) and to the horizontal wind drift of rain (Mittermaier et al., 2004; Harrold et al., 1974; Austin, 1987). Especially the effect of wind drift is still largely ignored in many operational applications. Instead, measured precipitation fields are projected to the ground level without any horizontal advection. For plenty of applications the accuracy of this projection is sufficient. For some applications, however, it is key to know exactly the location and the amount of precipitation that will reach the ground. Water utilities for example are responsible for managing precipitation runoffs to avoid flooding. They manage an extensive storm drainage system and rely on precise weather radar information. Insurance

companies might not pay for damages if radar images deceptively show that the precipitation event took place a significant distance away. For that matter, the impact of wind drift should be captured as precisely as possible.

The impact of wind drift has been already investigated in some studies. For snow and ice, wind drift values of 10–20 km at ranges of more than 100 km to the radar site have been found (Mittermaier et al., 2004). Lauri et al. (2012) suggest wind drift values at high elevation angles in snowfall might even exceed 100 km at ranges of 100–250 km to the radar site. For liquid precipitation they find horizontal displacements on the order of tens of kilometers, even at low elevation angles of 0.3° . These wind drift values have been calculated using only Met Office mesoscale model wind profiles, a profile of drop fall speeds to calculate horizontal displacements and radar measurements at a horizontal resolution of 500 m. Collier (1999) found that the impact of wind drift on radar measurements differs, depending on the radar resolution. They concluded that when ignoring wind drift, increasing the radar resolution to a certain point might actually decrease the accuracy. As the horizontal resolution of operational weather radars increases with time, this emphasizes the need for a reliable wind drift correction. There are only few studies attempting to correct the wind drift induced error. Harrold et al. (1974) found that correcting radar measurements by using only surface winds would already significantly decrease the discrepancies between radar and rain gauge measurements. Sandford (n.d.) discusses a wind drift correction that shows skill for medium and low rain rates but only for low resolution radars. Sandford (2015) evaluates different correction algorithms but found none of the available algorithms to be satisfying and suggests further research.

After a major radar system exchange that ended in 2015, the Deutscher Wetterdienst (DWD) now maintains a comprehensive network of 17 dual polarized Doppler radars with a 5-minute volume scan strategy (Helmert et al., 2014). This volume scan includes scans at elevation angles ranging from 0.5° to 25° . Each of these radars also provides a precipitation scan with a horizontal res-

olution of 250 m. The data of this radar network covers large portions of the troposphere with beam heights of up to 25.5 km. So far, all attempts to correct the effect of wind drift are based on models to simulate the trajectory of water droplets under the effect of wind drift. By utilizing the volume scan data of the DWD it becomes possible to directly observe the drift of precipitation fields rather than physically modeling the trajectory of precipitation. In several studies it is also suggested that the wind induced error becomes larger and more difficult to correct for high resolution radars (Sandford, n.d., 2015; Collier, 1999). With a horizontal resolution of 250 m, the precipitation scan of the DWD radar network is high resolution compared to the typical weather radar resolution of 1 km, which allows to determine the impact of wind drift on high resolution. Thus, this data bears the opportunity to answer the leading question of this thesis:

What is the impact of wind drift on radar-derived rainfall estimates?

To answer this question, the thesis is structured into 5 chapters. First of all, the available radar data and the associated radar setup is described in chapter 2. The analysis of this data and the applied algorithms to quantify the wind drift directly from radar measurements are described in chapter 3. For comparison to a more theoretical approach, chapter 4 presents a simple advection scheme that calculates a droplet size dependent trajectory to simulate falling precipitation fields under the effect of wind drift. Finally, the conclusions and an outlook are presented in chapter 5.

Chapter 2

Data

All data within this work is based on volumetric and dual polarized Doppler radar data. This data was provided by the DWD. They maintain a radar network in Germany that consists of 17 dual polarized Doppler radars of identical structure. The radar setup, the scan strategy and some radar characteristics of these radars are described in section 2.1. The impact of wind drift is analyzed based on six precipitation events in June 2016 that were featured by very strong precipitation. These events are described and characterized in section 2.2.

2.1. Volumetric Radar Data

It is essential to have access to volumetric radar data to be able to directly observe the effect of wind drift on radar measurements. In general, all radars that scan the atmosphere at different elevation angles are able to provide volumetric radar data. For this work, the volumetric data was provided by the DWD radar network. The DWD maintains a comprehensive radar network of 17 dual polarization radars, completely covering Germany (Figure 2.1). Out of this network only the data of the radar closest to Hamburg was taken into account. This is the radar located at 54.0055° N, 10.04683° E in Boostedt, which is roughly 30 km north of Hamburg. All radars of the network are polarimetric Doppler radars from the company EEC (USA) and with the

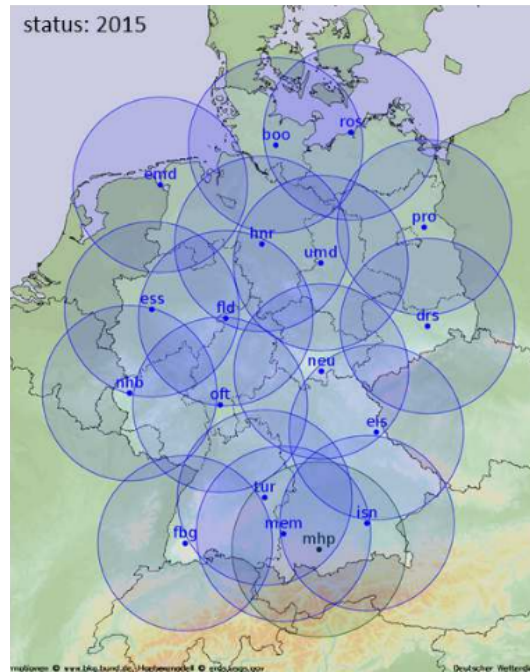


Figure 2.1: Radar network of the DWD (Helmert et al., 2014).

type “DWSR/5001/SDP/CE” (Figure 2.2). At a height of 124.6 m over sea level, the radar in Boostedt sends horizontally as well as vertically polarized waves into the atmosphere. With a wavelength of 5.3 cm, it falls into the category of C-Band radars. The radar measures at a beam width of 0.88° and a pulse width of $0.41 \mu\text{m}$. Only the horizontally polarized waves are considered as no hydrometeor classification will be done and horizontally polarized waves return generally a stronger echo due to the flattening of rain droplets. The scan strategy applied by the DWD repeats every five minutes and includes a precipitation scan, a volume scan and a 90° -scan for calibration purposes (Figure 2.3). The precipitation scan measures at the lowest elevation possible while following the orography and has a horizontal resolution of 250 m. The volume scan consists of scans at ten different elevations between 0.5° and 25° , each with a horizontal resolution of 1 km. For each scan, the radar antenna runs a full rotation over all azimuth angles at an angular resolution of 1° . Table 2.1 shows the duration, elevation, range and antenna speed of



Figure 2.2: Setup of the DWD radar. On the left side: Radar in Offenthal with radome and four lightning rods. On the right side: Radar without radome (Deutscher Wetterdienst, n.d.).

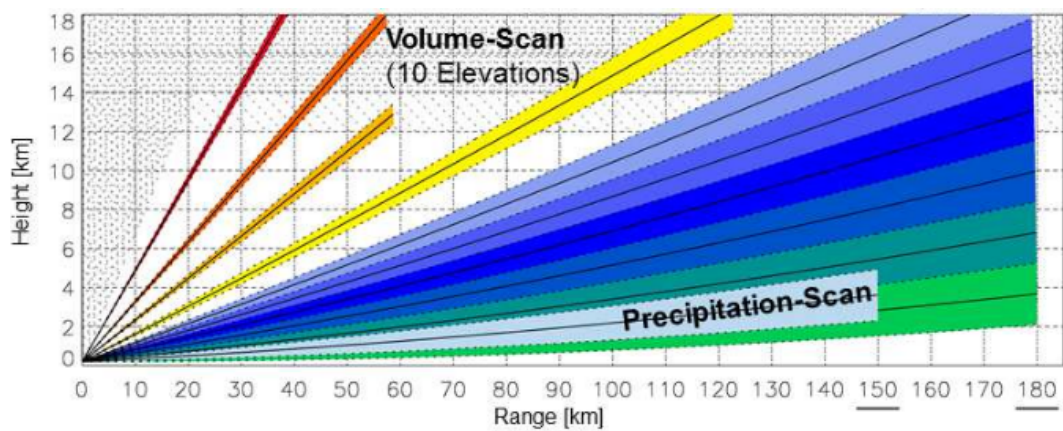


Figure 2.3: Scan strategy of all radars from the DWD radar network. The propagation of radar beams from the radar antenna is depicted. Each color belongs to a different elevation. These elevations are in ascending order: 0.5° , 0.8° (Precipitation-Scan), 1.5° , 2.5° , 3.5° , 4.5° , 5.5° , 8° , 12° , 17° and 25° (Helmert et al., 2014).

Table 2.1: Scan strategy of the DWD.

Time (s)	Elevation (°)	Range (km)	Antenna speed (rpm)
0 - 30	Precip.	150	2
32 - 55	5.5	180	2.6
56 - 78	4.5	180	2.6
79 - 102	3.5	180	2.6
103 - 125	2.5	180	2.6
126 - 149	1.5	180	2.6
150 - 180	0.5	180	2
182 - 202	8	124	3
205 - 217	12	60	5
218 - 230	17	60	5
232 - 242	25	60	5
243 - 299	Calibration	–	–

all scans. The DWD maintains an extensive software package for quality control of radar products called “**POL**Arimetric **R**adar **A**lgorithms” (POLARA). The quality control includes two steps: Radar signal processing at the radar site and post-processing in the central office in Offenbach. The available data for this work was corrected using only the signal processing at the radar site. This included I-Q data based Doppler filtering and Second Trip filtering. Furthermore, thresholds for Noise, Signal Quality Index, Signal Power, Clutter Power, Copolar Correlation Coefficient and Speckle filtering have been applied to filter clutter and other unrealistic data (Werner, 2014). The data that was corrected using only signal processing is the starting point for all analyses in the following chapters 3 and 4 (Figure 2.4).

2.2. Six Precipitation Events

Six different precipitation events were chosen to analyze the impact of wind drift on the rainfall estimates of the DWD radar. For later reference, each event will be identified with a letter from a) to f). Table 2.2 lists each event with

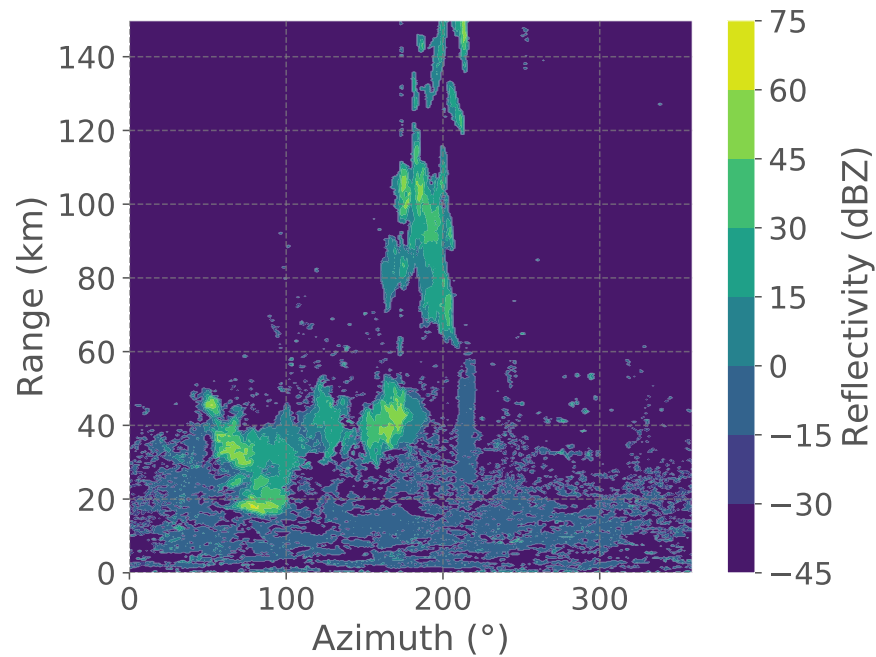


Figure 2.4: Example of the original data provided by the DWD.

its identifier, date, time and the corresponding wind measurement at the Wettermast Hamburg. The Wettermast Hamburg is a 305 m high weather mast, which is located in Billwerder, at the easterly outskirts of Hamburg (Brümmer et al., 2012). Along with other meteorological quantities, the Wettermast Hamburg provides precipitation measurements at the ground and wind measurements at several heights up to 280 m. The events were chosen upon the recommendation of A. Kuchenbecker (Hamburg Wasser, personal communication, June 02, 2017) as in all of these events flooding of the storm drainage system occurred to a small extent due to exceptionally strong precipitation and, perhaps, wind drift. Figure 2.5 shows the corresponding precipitation scan of the DWD radar in Boostedt. In all six events, strong precipitation was present over large parts of the radar’s measurement range. Especially noteworthy is event a), where not only strong precipitation was present at that time but also the formation of a tornado was confirmed (Hoffmann et al., 2018).

Table 2.2: Date, time and mean 10-min wind at 280 m height at the Wettermast Hamburg of the six precipitation events.

Event	Date (M-D-Y)	Time (UTC)	Wind speed	Wind direction
a)	06-07-2016	16:20	5.48 m s ⁻¹	244.14°
b)	06-13-2016	22:00	6.7 m s ⁻¹	185.48°
c)	06-14-2016	13:40	2.81 m s ⁻¹	170.95°
d)	06-17-2016	10:00	0.88 m s ⁻¹	141.68°
e)	06-24-2016	00:20	19.02 m s ⁻¹	258.95°
f)	06-25-2016	07:40	3.44 m s ⁻¹	12.32°

The measured winds at 280 m for each event are listed in Table 2.2. These measurements are also taken from the Wettermast Hamburg. Most events are associated with weak winds of 0.88 m s⁻¹ to 6.7 m s⁻¹. Solely event e) is characterized by strong winds of 19.02 m s⁻¹ at 280 m height. For the events b), c) and d), southerly wind directions were measured, while the events a) and e) had southwesterly winds and only the event f) is characterized by a northerly wind direction. Since this data is collected at one single location, it is by no means representative for the whole area covered by the DWD radar. Nevertheless, it is a good indicator for the current state of the atmosphere and useful to compare the magnitude of wind drift to the actual measured wind speed. For wind data higher than 280 m, soundings at the closest launching time from the nearest location Schleswig are shown in Figure 2.6 up to 450 hPa. Schleswig is located roughly 100 km north of Hamburg and lies within the range of the DWD radar in Boostedt. The soundings indicate without exception a fairly saturated atmosphere and within most of the free atmosphere the wind is rather constant, in speed and in direction. Exceptions are event d), where the wind direction changes from north over west to south and to a smaller extent event e), where northerly winds have been measured at 700 hPa in an otherwise northeasterly wind profile within the free atmosphere.

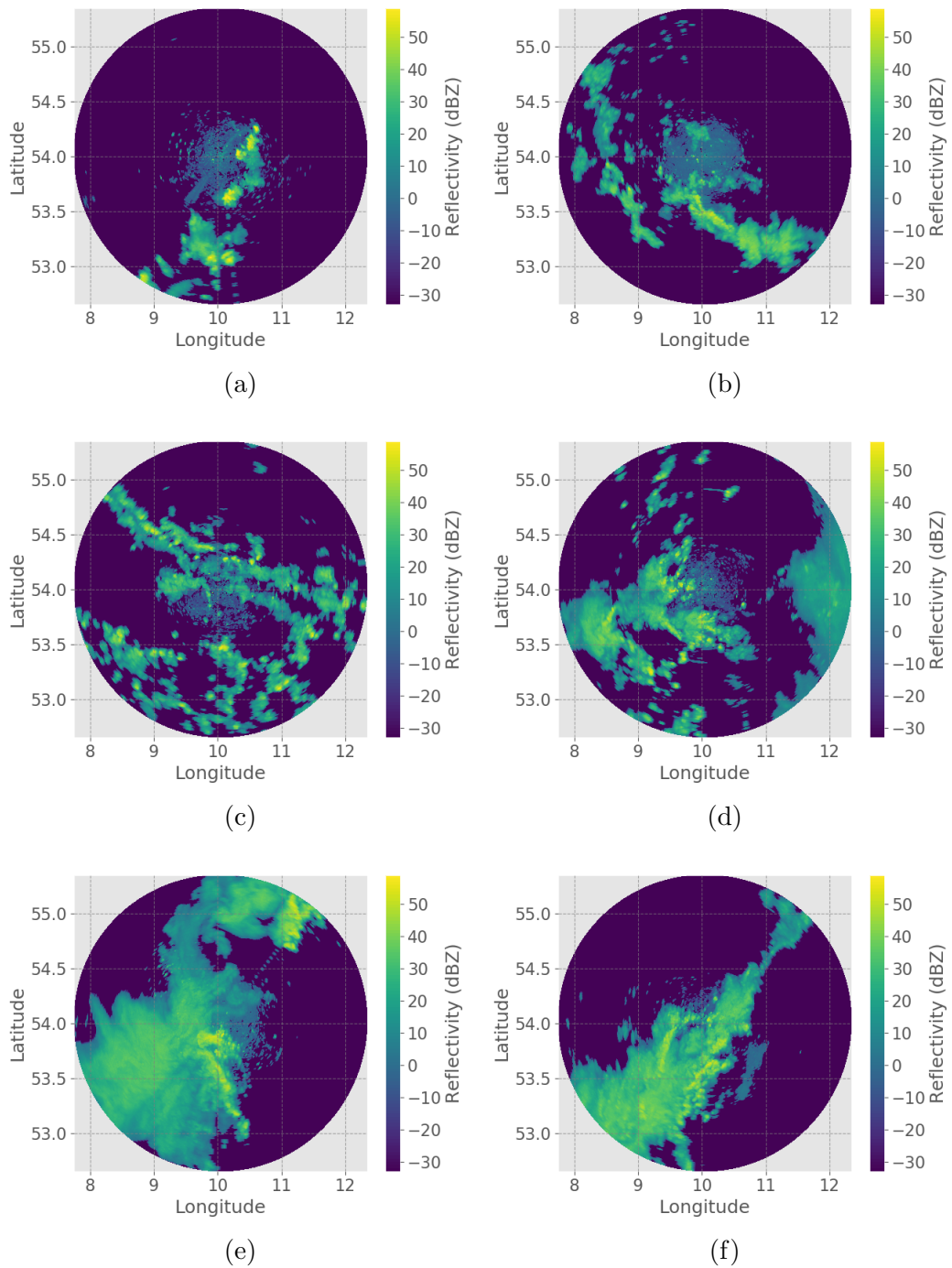


Figure 2.5: Precipitation scans for the six precipitation events in June 2016: a) June 7th at 16:20 UTC, b) June 13th at 22:00 UTC, c) June 14th at 13:40 UTC, d) June 17th at 10:00 UTC, e) June 24th at 00:20 UTC, f) June 25th at 07:40 UTC.

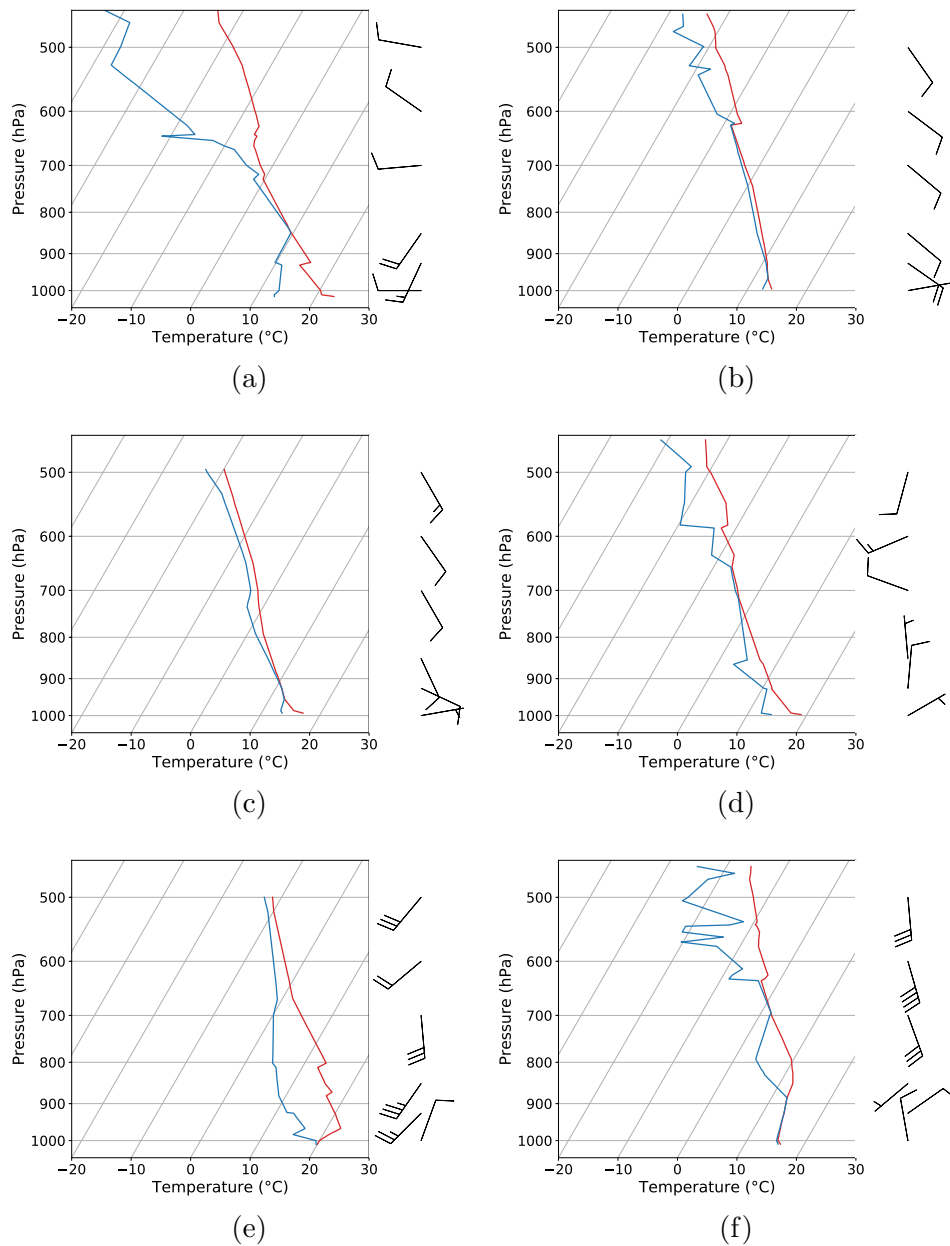


Figure 2.6: Soundings from Schleswig at closest launching times to the precipitation events: a) 2016-06-07 12 UTC, b) 2016-06-14 0 UTC, c) 2016-06-14 12 UTC, d) 2016-06-17 12 UTC, e) 2016-06-24 0 UTC, f) 2016-06-25 12 UTC. Temperature in red, dew point temperature in blue. Wind barbs in knots. Short and long barbs equal 5 kn and 10 kn respectively. Data from the University of Wyoming (University of Wyoming, n.d.).

Chapter 3

Analysis of Volumetric Radar Data

The DWD provides radar data of dual polarized C-Band radars which are able to scan the atmosphere at several different elevation angles. The scan strategy of these radars includes not only a precipitation scan but also a volume scan of measurements at ten different elevation angles. As a result, the volume around a radar site is covered with precipitation measurements at heights ranging from 0 up to 25.5 km. This is valuable data because the comparison of precipitation fields at different heights reveals the horizontal displacement, which is – by definition – the wind drift. For this reason, the following chapter focuses on utilizing the DWD data to calculate wind drift. At first, an algorithm is presented in section 3.1 to find the wind drift by matching images of precipitation at different heights against each other. This algorithm is referred to as the Precipitation Matching Algorithm. In the following section 3.2 this algorithm is then applied to the six precipitation events described in section 2.2 to obtain the wind drift values for some real precipitation events.

3.1. Precipitation Matching Algorithm

The wind drift between two heights can be found by matching the precipitation field at the lower height against the precipitation field at the upper height. By shifting the lower precipitation field into varying horizontal directions and with varying distances, the horizontal displacement that correlates best with the up-

per precipitation field can be found. This procedure to find wind drift between two heights is a template matching approach and works only on a regular grid. This is why the radar data will be interpolated to a three dimensional regular Cartesian grid first. The interpolation is implemented using Linear Barycentric Interpolation, which is a very fast method that uses a constant number of data points for the interpolation and is easy to implement also for higher dimensions. Since the interpolation to a grid point depends on the distance to the surrounding data points, the data points must be located very accurately within the Cartesian grid. To account for the earth's curvature, the coordinates of the data points are transformed to Cartesian coordinates by using the Transverse Mercator projection, which is a widely used and angle preserving map projection. The coordinate transformation will be described in part 3.1.1, followed by the interpolation to the Cartesian grid in part 3.1.2. Afterwards, in part 3.1.3, the template matching algorithm is applied. It matches the precipitation fields of different heights against each other to find the horizontal displacement at which a correlation reaches its maximum. Except for the area directly at the radar site, there are no radar measurements at ground level. As a result, the template matching algorithm cannot generally calculate the wind drift relative to the ground. To solve this problem, the horizontal displacement is calculated for several heights to obtain a relative drift profile between a base height and varying upper heights. This profile is then linearly extrapolated to the ground in part 3.1.4. The linear drift profile expresses only a relative drift between precipitation fields of different heights at the same time stamp. To obtain the real wind drift that the precipitation field has experienced while falling, the measured horizontal travel distance of the precipitation field at the upper height must be included (Part 3.1.5). This procedure as a whole will be referred to as the "Precipitation Matching Algorithm" in the following sections.

3.1.1. Coordinate Transformation

To find the shift between two heights using a template matching approach, the data must be available on a regular Cartesian grid. However, one drawback of a Cartesian grid is that it is based on a plane. For coordinate transformations from a spheroid to a plane, for example when locating Hamburg or a radar measurement within the new defined Cartesian grid, a map projection is needed. There are plenty of map projections available, each with its advantages and disadvantages. For this work the Transverse Mercator (TM) projection was chosen, a cylindrical map projection that is widely used and conformal. This means that the angles are preserved correctly. Although distances and areas are not preserved, the error stays within a few nanometers as long as the map does not exceed the 6-degree band of longitude where the TM projection is valid (Karney, 2011).

A radar measurement naturally available in polar coordinates will then be transformed to the target grid by the following process:

First, the great-circle distance or arc distance s_{arc} of the measurement to the radar is determined. The great-circle distance describes the distance along the surface of a sphere and is calculated according to Doviak and Zrnic (2006):

$$s_{\text{arc}} = k_e a \arcsin \left(\frac{r \cos \theta}{k_e a + h} \right) . \quad (3.1)$$

Here, $a=6\,370$ m represents the earth's radius, r and h are the measurement's range and height above ground, θ is the elevation angle and $k_e=4/3$ is a factor that accounts for the atmosphere's refractivity. This factor technically is wavelength-dependent, but for most weather radars a value of $k_e=4/3$ is a good approximation (Doviak and Zrnic, 2006).

By following Doviak and Zrnic (2006) again, the height h above ground is calculated as

$$h = \sqrt{r^2 + (k_e a)^2 r k_e a \sin \theta} - k_e a . \quad (3.2)$$

Next to the atmosphere's refraction, this formula takes also the earth's curvature into consideration.

Before applying the TM projection, the great-circle distance s_{arc} must be transformed to Cartesian distances:

$$x = s_{\text{arc}} \cos\left(\frac{\pi}{2} - \alpha\right) \quad (3.3)$$

and

$$y = s_{\text{arc}} \sin\left(\frac{\pi}{2} - \alpha\right), \quad (3.4)$$

where α is the measurement's azimuth angle in radians. By using the great-circle distance s_{arc} , it is ensured that the Cartesian distances x and y are distances along the earth's surface.

Finally, the Cartesian distances to the radar site are transformed to Cartesian coordinates within the TM projection¹. Together with the height according to eq. (3.2), the coordinates of measurements can then be provided in three dimensional Cartesian Coordinates. The coordinate transformation ensures that locations on the curved earth surface are located very accurately within the plane Cartesian grid. The error that would be induced by skipping the coordinate transformation is assumed to be very small. This means the coordinate transformation is not a necessity, but it is included to ensure the maximum possible accuracy.

3.1.2. Interpolation

To be able to apply the template matching algorithm, a regular Cartesian grid is necessary. This Cartesian grid is centered around the radar site. It has a horizontal and vertical resolution of 200 m and extends far enough to

¹The TM projection was implemented using the "Geospatial Data Abstraction Library" and its python module "osgeo.osr" (Warmerdam, 2008). For further information on this, the reader is referred to its official documentation: "gdal.org/python/".

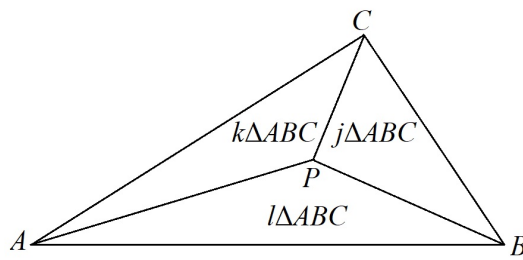


Figure 3.1: Barycentric Coordinates j , k and l of a point P . A , B and C are the data points of the surrounding triangle. ΔABC means the area of the whole triangle, while $l\Delta ABC$, $k\Delta ABC$ and $j\Delta ABC$ are the areas of the internal triangles. Image according to Vince (2017).

cover the 180 km range of the DWD radar. After the coordinates were transformed using the TM projection, the data is interpolated to this grid using Linear Barycentric Interpolation, which is basically a linear interpolation using Barycentric Coordinates². Rather than locating a point relative to an origin, Barycentric Coordinates locate a point relative to other, already existing data points (Vince, 2017). This holds the advantage that information about the distance between grid and data points is already included and does not need to be calculated anymore, which speeds up the interpolation. This procedure also makes sure that always the same number of data points are used for the interpolation. Barycentric Coordinates can be applied in several dimensions. The example below demonstrates the use of Barycentric Coordinates for linear interpolation in two dimensions, but the volume scan data actually consists of three dimensional data. The calculation of Barycentric Coordinates in three dimensions is analogous to two dimensions, except that a point is then located within a Tetrahedron instead of a triangle so that the Barycentric Coordinates are ratios of volumes instead of areas. In two dimensions, a point is located within a triangle of data (Figure 3.1). The Barycentric Coordinates are not only indicating the position of a point relative to the surrounding data, they are also proportional to the corresponding triangle area. In Figure 3.1 for ex-

²The Linear Barycentric Interpolation was implemented using python and the “LinearNDInterpolator” of the “scipy”-module (Jones et al., 2001)

ample, the area of the internal triangle ΔBCP decreases as the distance of the point P to the corner A increases. This is why Barycentric Coordinates are also known as areal coordinates. Sticking to the denotation of Figure 3.1, Barycentric Coordinates for a point within a 2D area are given according to Vince (2017):

$$j = \frac{\Delta BCP}{\Delta ABC} , \quad (3.5)$$

$$k = \frac{\Delta CAP}{\Delta ABC} . \quad (3.6)$$

$$l = \frac{\Delta ABP}{\Delta ABC} , \quad (3.7)$$

Here, ΔABP , ΔBCP and ΔCAP are the areas of the three internal triangles from Figure 3.1.

Since Barycentric Coordinates hold information about the distance of a point P to surrounding data points, the use of these coordinates provide a simple way for linear interpolation:

$$\mathbf{P} = j\mathbf{A} + k\mathbf{B} + l\mathbf{C} , \quad (3.8)$$

where \mathbf{P} is the interpolated value at the point P , and \mathbf{A} , \mathbf{B} and \mathbf{C} are the values at the data points of the surrounding triangle (Vince, 2017).

For the location of a point in Barycentric Coordinates, a surrounding grid of data points is necessary. In three dimensions, the data must be triangulated to a grid of Tetrahedron before applying Linear Barycentric Interpolation becomes possible in the first place. A method known as “Delauney Triangulation” was used for this task³. This method triangulates the data so that no point lies within the circumsphere of any Tetrahedron. For more information on the Delauney Triangulation, the reader is referred to detailed introductions by Preparata and Shamos (2012) or o’Rourke (1998).

³The Delauney Triangulation was implemented using “qhull” (Barber et al., 2013)

Using Linear Barycentric Interpolation, it is technically possible to interpolate data to grid points above the highest radar beam. In the vicinity of the radar, however, the radar beams of the volume scan are still close to the ground. At 5 km distance to the radar site for example, the radar beam with the highest elevation of 25° just exceeded a height of 2 km, while the predefined Cartesian grid reaches possible heights of more than 5 km, depending on the grid initialization. To prevent interpolations over these far distances, the interpolation was limited to grid points below to the highest radar beam. Below the lowest beam there is no interpolation possible because then it is not possible to find surrounding Tetrahedron anymore. As a result, the interpolation is limited to all grid points that are located between the lowest and the highest radar beam. Figure 3.2 shows an example of volume scan data interpolated to the 3D-Cartesian grid. Due to the display of a three dimensional volume on a two dimensional image, only the maximum values along each axis are displayed. The interpolation is applied in units of the relative reflectivity factor Z (Doviak and Zrnic, 2006):

$$\frac{Z}{\text{dBZ}} = 10 \log_{10} \frac{z}{\text{mm}^6 \text{ m}^{-3}}, \quad (3.9)$$

where z is the reflectivity factor in $\text{mm}^6 \text{ m}^{-3}$.

After the Linear Barycentric Interpolation was applied, the data is available on a three dimensional Cartesian grid. It is now possible to simply cut out a plane of a specific height from this grid. This plane is commonly referred to as “Constant Altitude Plan Position Indicator” (CAPPI, Figure 3.3). The advantage of using a CAPPI instead of a normal Plan Position Indicator (PPI) from a single radar beam is that there is no altitude changing with distance to the radar. The CAPPI at 1000 m height (Figure 3.3a) extends not nearly as far as the CAPPI at 5000 m height (Figure 3.3b). This is due to the lowest radar beam intersecting the 1000 m height plane at distances a lot closer to the radar site compared to the 5000 m height plane. Most of the area of the 1000 m plane is below the lowest radar beam and not considered for the

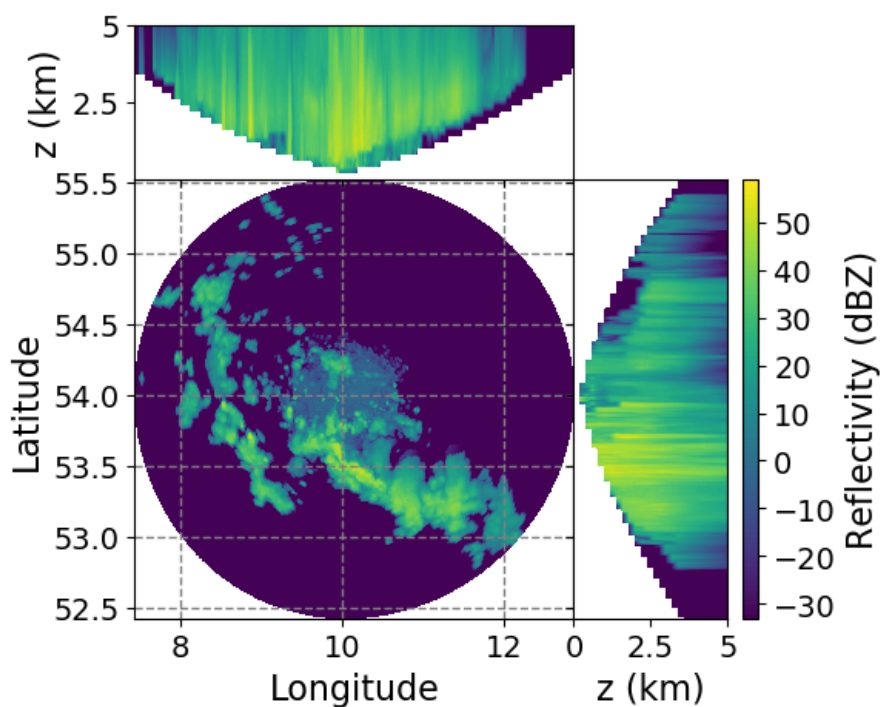


Figure 3.2: Reflectivity of event b), after interpolation to a three dimensional Cartesian grid. Center: Maximum reflectivity along the height-axis. Top: Maximum reflectivity along the Latitude-axis. Right: Maximum reflectivity along the Longitude-axis.

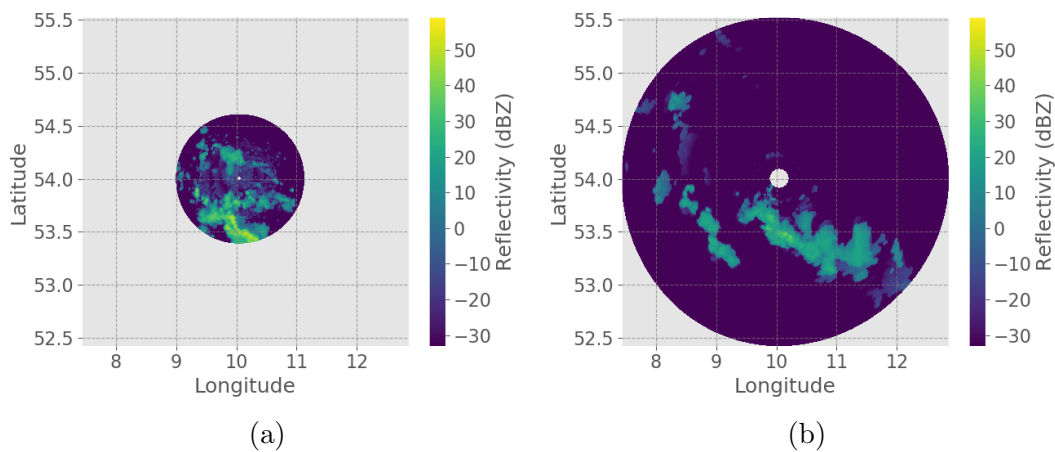


Figure 3.3: CAPPI at a) 1000 m height and b) 5000 m height for the event b).

interpolation method. This is also why there cannot be a CAPPI at ground level as there is no data at ground level and thus the complete area would be masked. Analogous, the masked area in the vicinity of the radar site is bigger for higher CAPPIs because then the highest radar beam intersects the plane further away from the radar site and more of the area around the radar vicinity is above the highest radar beam. This has less effect than the masked area below the radar beam. The upper Cartesian grid limitation of 3 km in the following sections results in only a small area masked in the vicinity of the radar for CAPPIs up to 3 km. Because there is only little data left for CAPPIs at very low heights the lowest CAPPI used in this work is set to 1 km height.

3.1.3. Template Matching

By constructing the CAPPIs, a tool has been created that allows the comparison of precipitation fields at two specific heights. Due to effects such as evaporation or coagulation, rain fields are not only horizontally drifted but change in intensity as well. Hence, the exact horizontal displacement cannot be calculated with absolute certainty. It is possible to calculate the most likely horizontal displacement by using a correlation measure to find the horizontal displacement of a lower CAPPI that matches the original CAPPI best. This is why the wind drift will be calculated using a template matching algorithm that uses “fast normalized cross-correlation” (Lewis, 1995) to find the displacement at which the cross-correlation between the two images is at a maximum. The cross-correlation is based on the squared Euclidean distance as the distance measure:

$$d_{f,t}^2(u, v) = \sum_{x,y} [f(x, y) - t(x - u, y - v)]^2 . \quad (3.10)$$

Here, f is the upper image. x and y are the Cartesian coordinates of the window containing the lower image t positioned at u, v . For no horizontal displacement, u and v would have a value of 0. By centering and normalizing

the images f and t to unit length, the normalized cross-correlation is obtained:

$$\gamma(u, v) = \frac{\sum_{x,y}[f(x, y) - \bar{f}_{u,v}][t(x - u, y - v) - \bar{t}]}{\{\sum_{x,y}[f(x, y) - \bar{f}_{u,v}]^2 \sum_{x,y}[t(x - u, y - v) - \bar{t}]^2\}^{0.5}}, \quad (3.11)$$

where \bar{t} is the mean of the lower image and \bar{f} is the mean of the upper image in the window containing the lower image. The fast normalized cross-correlation of Lewis (1995) calculates the normalized cross-correlation γ especially fast by using precomputed tables containing the integral of f and f^2 over the window of the lower image t . By applying fast normalized cross-correlation for all possible horizontal displacements, a correlation matrix for these displacements is created (Figure 3.4). The likelihood of a horizontal displacement is given by the normalized cross-correlation which means that the most likely horizontal displacement is at the point of maximum normalized cross-correlation. The gradient of the normalized cross-correlation is indicating the uncertainty of this algorithm. When the maximum cross-correlation is found within an area of very similar values the uncertainty is large because other horizontal displacements have also a high likelihood. On the other hand, when there is a steep gradient, the likelihood of other horizontal displacements decreases rapidly.

There are missing values at all areas above the highest radar beam and below the lowest beam due to the interpolation limited to the area between the highest and the lowest beam (Part 3.1.2). The template matching algorithm cannot handle missing values since the Euclidean distance cannot be calculated for missing values. Filling the missing values with zeros or other constant numbers would lead to a large portion of the images filled with the same number. This results in higher cross-correlation values whenever some of the constants are matched because the Euclidean distance to the same number equals zero. Leaving missing values out of the calculation would lead to very much data thrown away because otherwise correct data would be dropped when either the lower or the upper image has a missing value. This is why, for this template matching algorithm, the Cartesian grid is interpolated completely (also

below the lowest and above the highest radar beams), and the regions below and above the volume scan are masked only after the correlation matrix was calculated. This means that interpolations over far distances are allowed for the region in the vicinity of the radar and at the outer edge of the area covered by the radar. The effect is similar to the error that would be induced by a Nearest-neighbor interpolation, where the value of a measurement is interpolated over larger distances until a closer measurement can be found. The interpolation in the region above the highest beam is applied by using the same Linear Barycentric Interpolation as explained in the previous part. Below the lowest radar beam, a simple Nearest-neighbor interpolation from the lowest radar beam is applied.

The displacement at which the correlation is maximum will be assumed to equal the relative drift between the two heights. It is to be expected that precipitation fields change more significantly in structure and intensity the longer they fall. Because of that the correlation of two CAPPIs close to each other (Figure 3.4a) is greater than the correlation of two CAPPIs that are separated by larger distances (Figure 3.4b).

The template matching algorithm is likely to fail for CAPPIs within or above the Bright Band due to the change of phase and the associated increase of reflectivity within the Bright Band. To minimize the error that is induced by the Bright Band, only CAPPIs up to a height of 3 km will be analyzed in the following sections. Since all analyzed precipitation events took place during the summer, the Bright Band is expected to be at high altitudes and thus, most of the heights up to 3 km should be below the Bright Band.

3.1.4. Profiles of Relative Drift

Since there are no radar measurements at ground level, it is not possible to calculate a CAPPI at ground level and thus, wind drift cannot be calculated relative to the ground directly. However, for plenty of applications, the precipitation at ground is most important. To solve this problem, the shift between

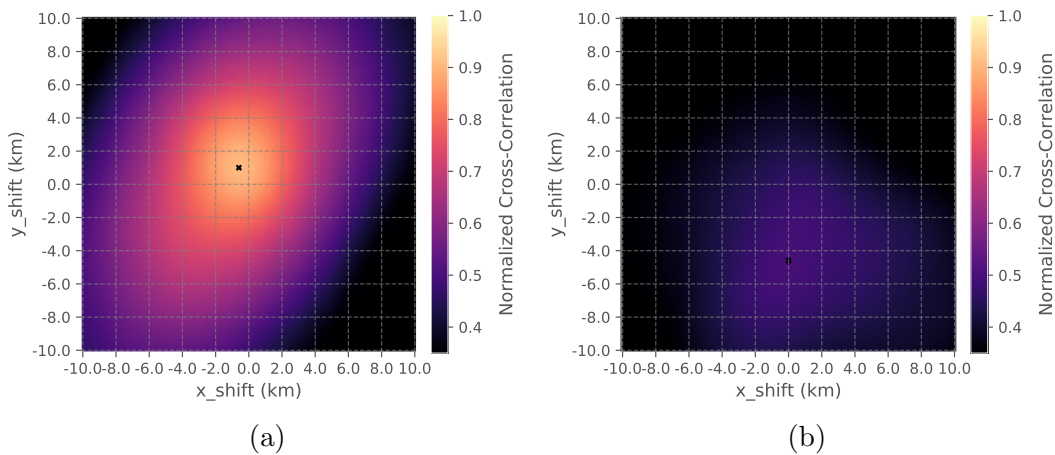


Figure 3.4: Normalized Cross-Correlation matrix for the precipitation event a). Axis label refer to horizontal displacement of the CAPPI at 1 km height, relative to the CAPPI at a) 2 km and b) 5 km height. The 'x'-symbol marks the horizontal displacement, at which the correlation is at its maximum.

a base CAPPI at 1 km and all CAPPIs above is calculated to obtain a profile of the relative drift to the 1 km CAPPI (Figure 3.5).

A maximum of 3 km height is chosen to allow the maximum height difference, while ensuring that almost all droplets are still in the liquid phase. To separate distance from direction, the profile of relative drift is divided into a profile of drift distance and a profile of drift direction. Both profiles are then linearly extrapolated to the ground by fitting a linear function to the profiles that minimizes the root mean squared error (RMSE). The available data shows only small deviations from the linear profile. The average RMSE equals 120 m and 2° for the distance and direction profile respectively (A more detailed analysis of the events is demonstrated in section 3.2). The small RMSEs justify the use of the linear fit.

As relative drift profiles are calculated relative to the base CAPPI at 1 km height, this results in a drift distance of zero at 1 km height and negative

drift distances at the ground. To obtain the drift relative to the ground, the condition of a relative drift distance of zero at ground level is applied. This is enforced by calculating the relative drift profile and extrapolate it to the ground. The offset to zero drift at ground level is then subtracted from all drift values of the relative drift distance profile (Figure 3.5c). Because both direction and distance of wind drift show only small deviations from a linear profile, the linear fitted function is used to extrapolate the drift profile to the ground. Using this fitted function, one can obtain drift values not only for heights between two CAPPs but also for the ground level. In theory, however, the wind profile changes within the boundary layer. The wind direction is usually not constant anymore, e.g. due to effects such as the Ekman spiral. Within the surface layer and in a neutrally stratified environment, the wind speed also changes to a logarithmic wind profile. Compared to a logarithmic profile, the linear extrapolation leads to higher drift distances at low heights. Thus, it is to be expected that the linear extrapolation results in slightly higher drift distances and to less change in the drift direction than the relative drift observed in reality. Due to time limitations, this effect is not further considered.

3.1.5. Calculation of Absolute Wind Drift

The absolute wind drift that a precipitation field experiences is the distance that the precipitation was horizontally displaced while falling to the ground. This means, there is a time difference between the precipitation field at the original height of 3 km and the corresponding precipitation field at ground level. However, the relative drift calculated in the previous part is the shift between the precipitation field at 3 km and the ground level at a single time step. For a stationary precipitation field at 3 km height, this is equal to the absolute wind drift between the ground and 3 km height because the precipitation field at the original height has not moved (Figure 3.6a). For non-stationary precipitation fields, the original precipitation field has horizontally moved while

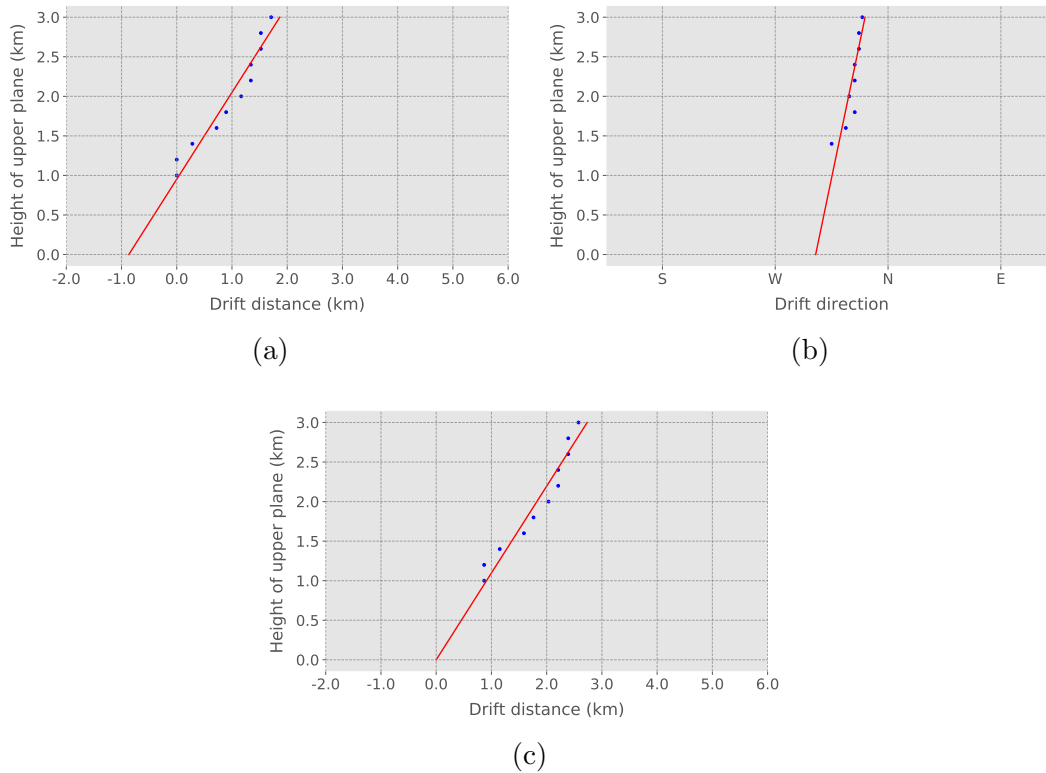


Figure 3.5: Profiles of relative drift to a base CAPPI at 1 km for the precipitation event a. a) Profile of relative drift distance. b) Profile of relative drift direction. c) Profile of relative drift distance with an offset added so that the drift distance at ground equals zero. Blue dots are drift values as calculated by the template matching algorithm. A linear least-squared fit is visualized as the red line.

the precipitation was falling to the ground and the relative drift is not sufficient anymore to obtain the absolute wind drift (Figure 3.6b). Thus, there is an essential difference between the relative drift as calculated in the previous part and the absolute wind drift that a precipitation field will experience while falling to the ground. A first intuitive solution to this problem would be to find the absolute wind drift directly by applying the template matching algorithm on the two associated CAPPIs at different times. The upper CAPPI at time t_0 would then be matched with the lower CAPPI at time t_1 so that the time difference between t_1 and t_0 would equal the fall time of the precipitation. However, the temporal resolution of the radar volume scan is only five minutes. This is a similar magnitude compared to typical fall times of precipitation with terminal velocities usually ranging between 1 m s^{-1} and 10 m s^{-1} , depending on the drop diameter. Within five minutes, the precipitation field might have moved already a significant horizontal distance. For example, at a horizontal speed of 10 m s^{-1} , the precipitation field would have moved 3 km already. This means, the absolute drift could only be resolved at steps of more than 3 km, which is too low to obtain meaningful results. This is why a different approach will be applied to calculate the absolute wind drift for non-stationary precipitation: The horizontal distance \vec{x}_t traveled by the precipitation field within the fall time is calculated and added to the relative drift \vec{d}_r to obtain the absolute wind drift:

$$\vec{d}_w = \vec{x}_t + \vec{d}_r . \quad (3.12)$$

The travel distance \vec{x}_t is assumed to be constant over all heights. It represents the travel distance of the fall streak as a whole. The relative drift \vec{d}_r to the ground is known from the linear drift profile. The travel distance of the precipitation field is calculated from the horizontal travel speed \vec{v}_h and the fall time t_f :

$$\vec{x}_t = \vec{v}_h \cdot t_f . \quad (3.13)$$

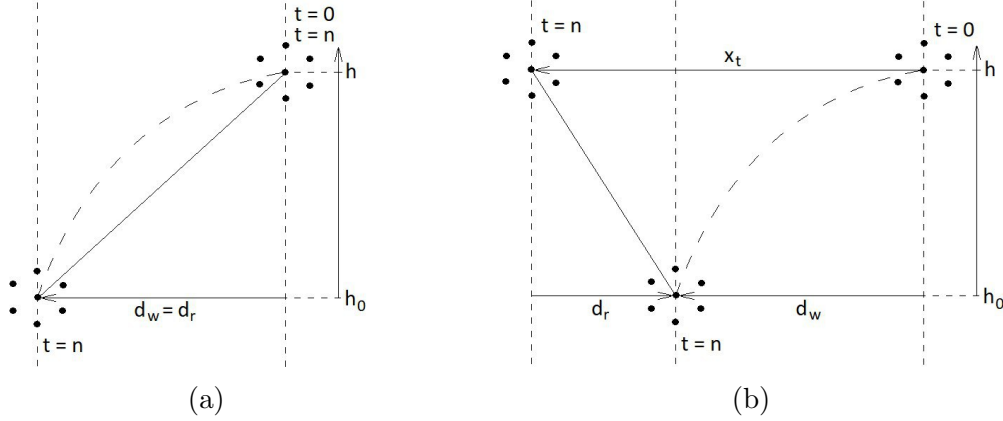


Figure 3.6: Relation between relative drift d_r , absolute wind drift d_w and travel distance x_t of a precipitation field within time from 0 to n . A precipitation field is illustrated as 7 black dots in a circular arrangement. Long dashes illustrate the precipitation trajectory while falling. a) Stationary precipitation fields. b) Non-stationary precipitation fields.

The travel speed \vec{v}_h is obtained by using the template matching algorithm from part 3.1.3. Instead of matching CAPPIS at different heights, this time CAPPIS at the same height but from different measurement times are matched. The resulting shift \vec{s} between the CAPPIS divided by the time Δt between the measurements yields the travel speed:

$$\vec{v}_h = \frac{\vec{s}}{\Delta t}. \quad (3.14)$$

The fall time of water droplets depends on the height of the droplets and the speed at which they fall to the ground. It is assumed that all droplets permanently fall at their terminal velocity. The terminal velocity is the velocity that a droplet reaches in equilibrium when all positive and negative forces are in balance so that the net force on the droplet is zero and there is no more acceleration. The terminal velocity is dependent on the drop diameter D . A precipitation field consists of many different drop diameters. Hence, the wa-

ter droplets of a precipitation field reach the ground after different fall times and there is no single fall time t_f for a precipitation field in reality. To obtain a single representative wind drift value for a precipitation field, a single representative value for the fall time is necessary. Such a representative fall time could be the fall time of the median volume diameter D_0 , which is exactly the drop diameter such that half the water is contained in larger drops (Doviak and Zrnica, 2006):

$$\left(\frac{\pi\rho_w}{6}\right) \int_0^{D_0} D^3 N(D) dD = \frac{M}{2} , \quad (3.15)$$

where $\rho_w=10^3 \text{ kg m}^{-3}$ is the density of water, M is the total liquid water content and $N(D)$ is the number of drops in $\text{mm}^{-1} \text{ m}^{-3}$ at the diameter D in mm. $N(D)$ is calculated according to Marshall and Palmer (1948):

$$N_D = N_0 e^{-\Lambda D} , \quad (3.16)$$

where the intercept $N_0=8 \cdot 10^3 \text{ mm}^{-1} \text{ m}^{-3}$ is the value of N_D for $D=0$ and Λ is the slope in mm^{-1} (Marshall and Palmer, 1948):

$$\Lambda = 4.1R^{-0.21} , \quad (3.17)$$

with R being the rainfall rate in mm h^{-1} . The rainfall rate R is derived from the reflectivity measurement according to Marshall et al. (1955):

$$R = \frac{z}{200}^{\frac{1}{1.6}} , \quad (3.18)$$

where z is the measurements reflectivity factor in $\text{mm}^6 \text{ m}^{-3}$.

Solving eq. (3.15) for the median volume diameter D_0 yields according to (Doviak and Zrnica, 2006):

$$D_0 = \frac{3.67}{\Lambda} . \quad (3.19)$$

The terminal velocity of a droplet is calculated according to (Atlas et al., 1973)

with a height dependent factor $\delta(h)$ according to METEK GmbH (2009):

$$v_t(h) = (9.65 - 10.3 \cdot e^{-0.6D}) \cdot \delta(h) , \text{ for } 0.109 \text{ mm} \geq D \geq 6 \text{ mm} , \quad (3.20)$$

$$\delta(h) = 1 + 3.36 \cdot e^{-5h} + 1.71 \cdot e^{-9h^2} , \quad (3.21)$$

where h is the height in m. The terminal velocity is height dependent. Hence, the fall time at height h is:

$$t_f(h) = \frac{\Delta h}{v_t(h)} . \quad (3.22)$$

To obtain the total fall time of droplets at the median drop diameter, the height dependent fall time of this drop diameter must be integrated over the total column height H :

$$t_{f,\text{total}} = \int_0^H t_f(h) dh . \quad (3.23)$$

Using this representative fall time, the final wind drift a precipitation field will experience while falling to the ground is then calculated according to eq. (3.12). In summary, the absolute wind drift between a height h and the ground is found using only the radar volume scan data in five steps:

1. Coordinate transformation taking the earth's curvature into consideration.
2. Linear Barycentric Interpolation to a three dimensional Cartesian grid.
3. Finding the most likely relative drift by template matching.
4. Linear extrapolation to the ground.
5. Calculation of absolute wind drift by adding relative drift to precipitation travel distance.

This procedure as a whole will be referred to as the Precipitation Matching Algorithm (PMA) in the following sections.

3.2. Application of the Precipitation Matching Algorithm

The previous section presented a method to calculate wind drift from radar volume scan data. In the following section, this method will be applied to six different precipitation events in June, 2016 which haven been described in section 2.2. In part 3.2.1, the relative drift to the ground is calculated for all 6 events by extrapolating relative drift profiles to the ground. By including the traveled horizontal distance of the original precipitation fields, the absolute wind drift is calculated for all events in part 3.2.2. The stability of the created relative drift profiles are examined in part 3.2.3 before finally, in part 3.2.4, the calculated wind drift will be used to correct the wind induced error of the DWD precipitation scan.

3.2.1. Resulting Relative Drift

To obtain the absolute wind drift for all precipitation events, the PMA must be applied on each event. The PMA consists of several steps (Part 3.1.5). After a coordinate transformation and interpolation of the data to a regular Cartesian grid, a relative drift profile is created within the PMA to obtain the relative drift to the ground for all precipitation events (Figure 3.7). Only events c) and e) are shown because they are representative for all other events. The relative drift profiles of all events can be found in Appendix A. The drift distance of the drift profiles monotonously increases with height for all precipitation events. This is somewhat surprising as the template matching algorithm has no information about the height but simply compares two images to find a displacement. Nonetheless, an increase of drift distance with height distance is in general to be expected because greater height distances lead to longer fall times, which means that the precipitation is longer exposed to wind drift. With heights of up to 3 km, most of the analysis happens within the free atmosphere, where the wind is nearly geostrophic (Etling, 2008; Holton and Hakim, 2012)

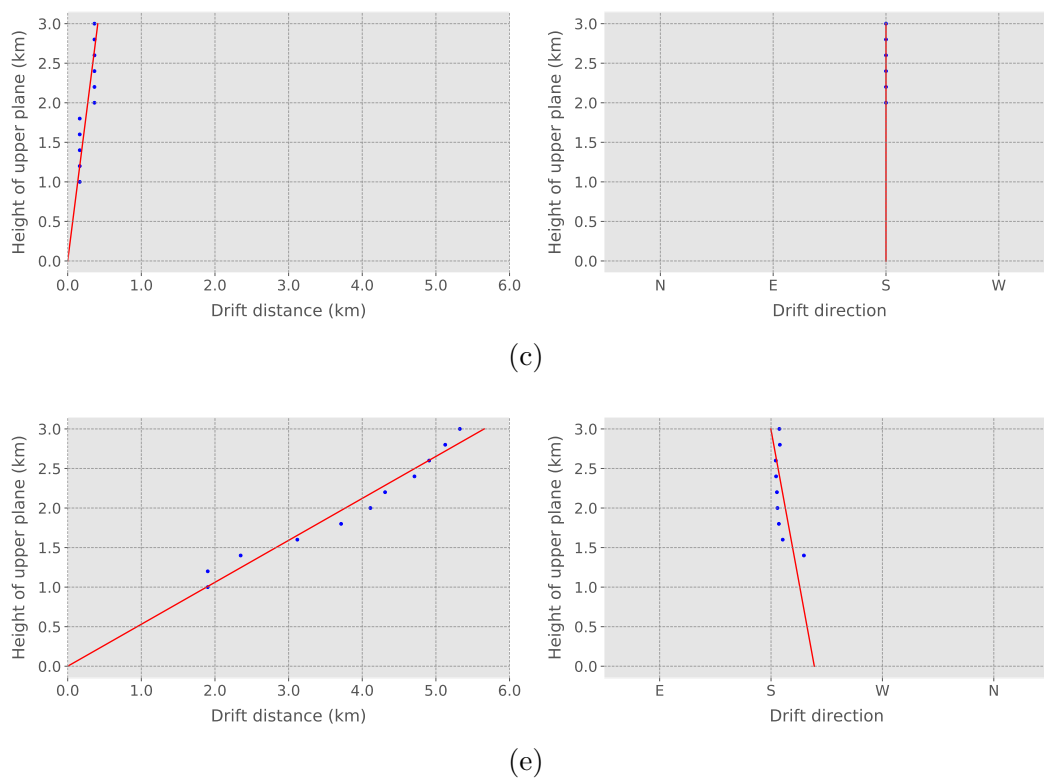


Figure 3.7: Same as in Figure 3.5, but for events c) and e) and with an offset added such that the relative drift relative to the ground equals zero.

and thus barely changes with height. However, a completely constant wind profile up to 3 km height is rarely observed in reality. Instead, the wind is likely to differ slightly between close heights and stronger for heights far away. The relation between height difference and wind difference appears to be linear in all cases, since the drift profiles of the precipitation events show only very little deviations from a linear profile with a mean RMSE for the relative drift distance of 120 m (Table 3.1).

Not only the drift distance profiles are characterized by linear behavior, also the drift direction has little deviation from a linear profile with a mean RMSE for the relative drift direction of 2° . Events b) and c) even have zero deviation from a linear profile (Figure 3.7c for the representative event c), event b) can

Table 3.1: RMSE of the relative drift profiles against a linear fit.

Event	Relative drift distance (m)	Relative drift direction ($^{\circ}$)
a)	130	3
b)	83	0
c)	41	0
d)	69	2
e)	205	5
f)	196	2

be found in Appendix A). In these cases, the relative drift direction stays constant up to 3 km height. The other events are characterized by a small change of the relative drift direction only. This is in agreement with the sounding measurements that are characterized by small changes in wind direction within the free atmosphere. However, the small changes could also indicate an error induced by a high vertical grid resolution in combination with a low vertical resolution of the radar beams. When neighboring radar beams of the volume scan are too far away, a high vertical grid resolution leads to neighboring CAPPIs being very similar. This is due to an interpolation from the same radar beam for large portions of the precipitation area. As a result, some of the constant relative drift values might be a consequence of the high vertical grid resolution in combination with a low vertical resolution of the volume scan. This should only be problematic for neighboring CAPPIs though. A constant drift direction profile up to 3 km height cannot be explained by the grid resolution and is more likely to be a consequence of the small change in wind direction within the free atmosphere. An improved vertical resolution of the radar beams, e.g. a volume scan consisting of more elevations would prevent this problem and allow even finer grid resolutions.

The calculated relative drift to the ground for the events a) to f) ranges between 0.4 km and 5.7 km (Table 3.2) with an average of 2.7 km for the six precipitation events. For stationary precipitation fields these values would

equal the absolute wind drift. Since precipitation fields are rarely stationary in reality, the next part focuses on calculating the absolute wind drift.

3.2.2. Resulting Absolute Wind Drift

By following the methodology presented in part 3.1.5, the absolute wind drift is calculated for all precipitation events according to eq. (3.12). This calculation depends on the median volume diameter and the travel speed of the precipitation fields, which are calculated for all events according to eq. (3.19) and eq. (3.14) respectively (Table 3.3). When comparing the relative drift with the absolute wind drift (Table 3.2), two differences become apparent: The absolute drift distances are greater than the relative drift distances for five of the six precipitation events and the absolute drift direction is in opposite direction compared to the relative drift direction for all events. For all six events, the absolute drift direction is different from the relative drift direction by values close to 180° . This means that the calculated travel speed of the precipitation field at the original height of 3 km is greater than horizontal drift speed of the falling precipitation. Whenever the travel distance of the original precipitation field is greater than the horizontal drift of the falling precipitation, the relative drift direction is necessarily of opposite direction. This is because the precipitation field at original height has traveled greater horizontal distances compared to the precipitation that arrives at ground level (Figure 3.6b). This is not surprising as the wind speed becomes usually greater with increasing height.

The absolute wind drift distance is in five of the six events greater than the relative drift distance. Solely for event e) a relative drift distance larger than the corresponding absolute wind drift distance was calculated. The relative drift distance is defined as the relative distance between the precipitation fields at 3 km height and ground at a single time step. This means the relative drift distance arises solely as a result of wind speed differences within the wind profile. Differences in wind speed are generally smaller than the total wind

Table 3.2: Relative and absolute drift between 3 km height and ground level.

Event	Rel. distance	Abs. distance	Rel. direction	Abs. Direction
a)	2.7 km	3.4 km	342°	72°
b)	0.9 km	2.6 km	135°	324°
c)	0.4 km	3.3 km	180°	20°
d)	2.2 km	1.0 km	221°	120°
e)	5.7 km	7.9 km	180°	49°
f)	4.6 km	4.7 km	194°	340°

Table 3.3: Median volume diameter, travel speed and fall time from 3 km height to ground level for the precipitation of events a) to f).

Event	Median volume diameter	Travel speed (m s^{-1})	Fall time (s)
a)	0.92 mm	5.7	766
b)	0.85 mm	4.3	821
c)	0.81 mm	4.2	864
d)	0.81 mm	3.0	864
e)	0.95 mm	16.8	742
f)	1.0 mm	12.7	696

speed which means that it is in general to expected that the absolute drift is greater than the relative drift. Event e) is an exception because there are very small total wind speeds associated with this event (0.88 m s^{-1} measured at the Wettermast Hamburg, Table 2.2).

The calculated absolute drift distances range between 1 and 7.9 km with an average of 3.8 km between 3 km and the ground for the six precipitation events. These are realistic magnitudes that are slightly below the wind drift magnitudes found by other studies. Harrold et al. (1974) for example found wind drift magnitudes of 1-2 km while falling from 500 m height, which is only one sixth of the fall distance compared to this study. Mittermaier et al. (2004) even found wind drift values of 10-20 km for precipitation originating from 2 km

above the Bright Band, although they had their focus on drift of snow and ice, which is generally drifted further due to lower fall velocities compared to rain droplets. When comparing the absolute drift calculated by the PMA to the synoptic environment, good agreement becomes apparent. The strongest winds have been measured by the Schleswig-sounding for event e), followed by event f), which are the events for which the PMA calculates the highest absolute drift distances of 7.9 km and 4.7 km respectively. These similar tendencies are a surprisingly good result and show that the wind drift can at least tententially computed using the PMA without any knowledge about the wind profile.

3.2.3. Stability of the Relative Drift Profiles

The relative drift profiles have been calculated from a single radar volume scan and are only valid within this volume scan, which takes five minutes to finish. To examine the stability of the wind drift, relative drift profiles from 30 minutes before the defined time stamp of each precipitation event to 30 minutes afterwards are created and the standard deviation of the relative drift is calculated. The time stamp of each precipitation event is listed in chapter 2 (Table 2.2). Since the radars temporal resolution is five minutes, there is a total of 13 volume scans included for the calculation of the standard deviation (The volume scan exactly at the time stamp of the event, the six volume scans before and the six volume scans afterwards). There is very little change in the relative drift profiles within this period of time for all precipitation events. The mean standard deviation over the precipitation events a) to f) equals 153 m and 8° for the wind drift distance and wind drift direction respectively (Table 3.4). Compared to the total relative drift distances (Table 3.2) this results in a relative standard deviation of 5% on average for the relative drift distances. This shows that there is not only little change in the synoptic wind environment but also that the PMA is very robust and will show similar results for similar synoptic environments. The standard deviation of the wind drift distance increases

Table 3.4: Mean standard deviation over the relative drift profile within 30 min before to 30 min after the precipitation event.

Event	Drift distance (m)	Drift direction (°)
a)	148	8
b)	43	18
c)	28	4
d)	76	3
e)	361	9
f)	262	7

slightly with height for most precipitation events (Figure 3.8 for event a), see Appendix A for events b) to f)). This is not surprising because with an increasing height distance the fall time increases too. This means that the precipitation field is more likely to change significantly within the fall time, which results in lower correlations between the upper and the lower precipitation field. This is an expected behavior from the PMA as explained at the end of part 3.1.3.

The standard deviation of the wind drift direction does not change much with height, except that the wind drift direction varies more strongly at the lowest levels (Figure 3.8). This is due to less data available for the wind drift direction at low levels. The PMA calculates more frequently a wind drift of 0 at low heights because the corresponding CAPPIs are close to each other and similar. When there is no drift detected, the drift distance is 0, but there is no associated wind drift direction. Thus, there is less data available for calculating the standard deviation of the wind drift direction at low levels, which increases the influence of outliers and results in higher variations.

3.2.4. Correction of Precipitation Scans

With the PMA at hand, a tool is available to calculate the wind drift that precipitation at height h would experience until reaching the ground. The ab-

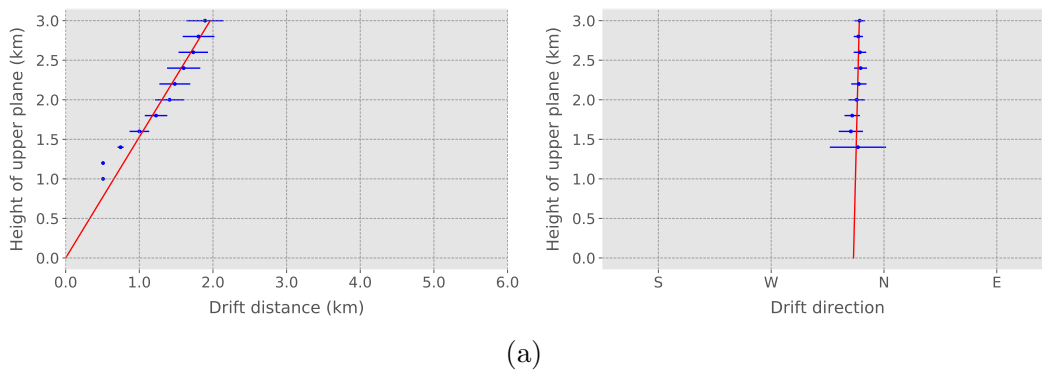


Figure 3.8: Standard deviation for wind drift profiles 30 minutes before and after the precipitation event a). Blue dots are the mean wind drift at that height, blue lines depict the standard deviation. On the left: Profile of wind drift distance. On the right: Profile of wind drift direction. A linear least-squared fit is visualized as the red line. An offset was added to all values of the distance-profile, so that the fitted drift distance at ground equals 0.

solute wind drift is the sum of relative drift and horizontal travel distance of the precipitation field. The relative drift is dependent on the height above ground, according to the linear drift profile. With information about the horizontal travel speed of the precipitation field and about the height of the precipitation measurements, a radar measurement can be corrected with the absolute wind drift to obtain a precipitation field at ground level that has been corrected for wind drift. To demonstrate this, the precipitation scan of the DWD radar will be corrected for wind drift in the following part.

The measurement bins along the beam of the precipitation scan are not constant in height though. Due to the radar beam's elevation angle, the height of a measurement bin increases with distance to the radar site. As a consequence, the fall time and the wind drift that the measured precipitation experiences when falling to the ground depends on the height of the corresponding measurement bin. That's why the wind drift that precipitation will experience is calculated for each measurement bin individually. The height of a mea-

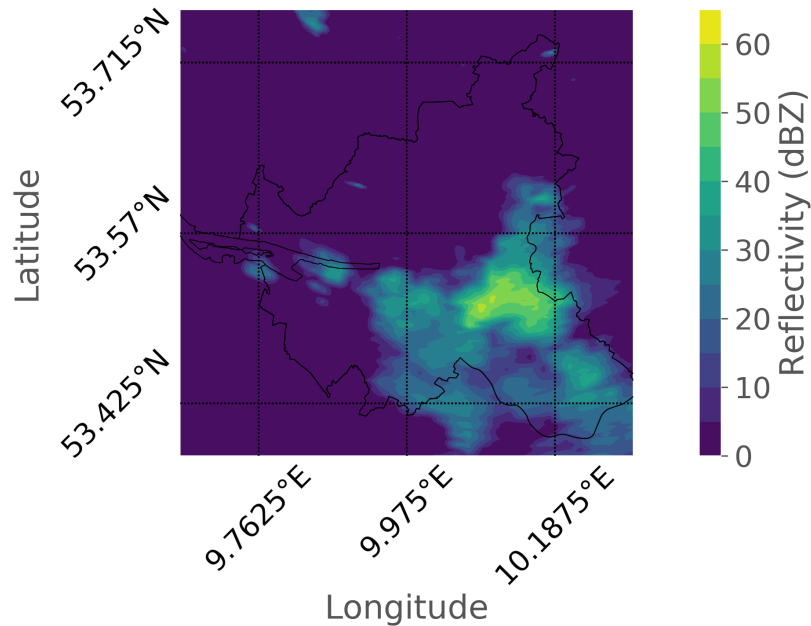


Figure 3.9: Corrected precipitation scan over Hamburg for event c)

surement bin is calculated according to eq. (3.2). Each measurement bin is then relocated to the ground with a horizontal drift according to the calculated absolute wind drift of the corresponding height. This relocation does not necessarily happen on a regular grid because the calculated wind drift is not limited to the grid resolution. To bring the relocated measurement bins to a regular grid, the relocated measurement bins are interpolated back to the regular Cartesian grid (Figure 3.9). This interpolation is again implemented by using Linear Barycentric Interpolation (Part 3.1.2). Since all measurements have been projected to the ground by applying the wind drift relative to the ground, this interpolation happens in two dimensions this time. This procedure assumes all droplets reach the ground at the same time. The implications of this assumption are discussed at the end of this section.

To highlight the differences between original and corrected radar image the difference at each grid point is calculated by subtracting the original reflectivity field from the corrected reflectivity field. Since the original reflectivity is

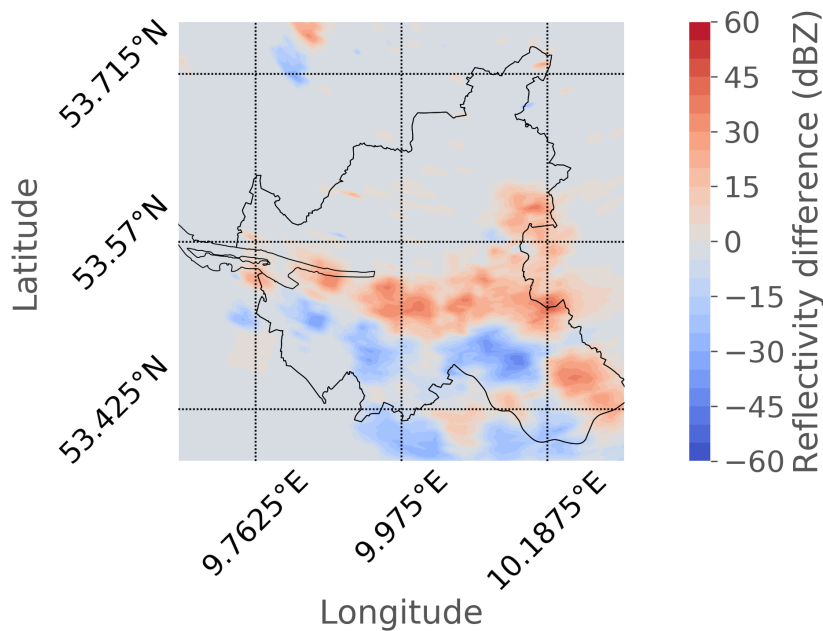


Figure 3.10: Difference between corrected and original precipitation scans over Hamburg for event c).

subtracted from the corrected reflectivity, precipitation drifted into an area is indicated by positive values, while negative values indicate that more precipitation has been drifted out of that area (Figure 3.10). When this is compared to the wind drift profile (Figure 3.11) one can see that the precipitation patterns are simply shifted into the wind drift directions from the wind drift profile. This is an expected behavior and shows that at least the direction of wind drift correction by the PMA was applied correctly. In case of event c) southeasterly winds have been measured which results in northeasterly wind drift directions. That's why, the red maxima in Figure 3.10 are always in the northeast of the blue minima (The difference plots of events a), b) and d) to f) can be found in Appendix A). This procedure assumes that all droplets reach the ground at the same time. This assumption is violated in reality due to two reasons. First of all, the measurement bins along a radar beam are not at constant height. Secondly, the droplets of a precipitation field have different fall velocities, de-

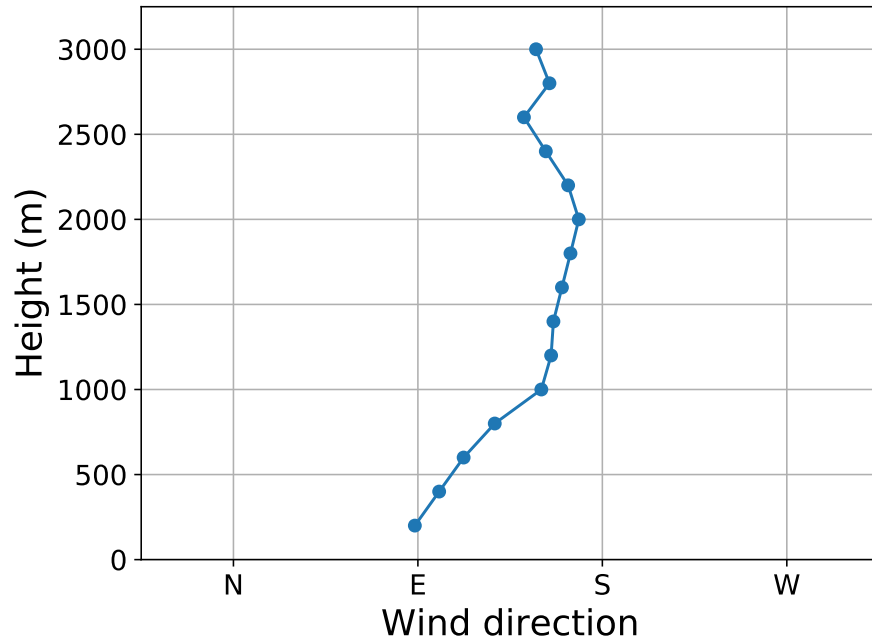


Figure 3.11: Wind direction profile of event c) measured by the Schleswig-sounding.

pending on the drop diameter. The error induced by the height difference of the measurement bins along the radar beam gets bigger with a greater elevation angle of the radar beam because then the height of the measurement bins vary more significantly. For radar images of constant height, e.g. CAPPs, the error is less significant because the droplets originate from a constant height. The assumption that all droplets reach the ground at the same time is still not valid because of the differences in fall velocity though. The correction of a radar image with wind drift could be further improved by correcting the wind drift for each drop size individually (spectral correction) and not by shifting the precipitation field as a whole (integral correction).

Chapter 4

A Simple Advection Scheme

In the previous chapter, wind drift was found by matching precipitation patterns of different heights. This way, a specific wind drift value for the wind drift between two heights could be calculated. The following chapter takes a theoretical approach to analyze wind drift. A simple advection model is presented that simulates falling droplets considering the effect of wind drift. To show the basic characteristics of wind drift, in section 4.1 this model is applied to some artificially created stationary rain fields first, followed by some measured rain fields in a stationary setup. Afterwards, also wind drift for non-stationary precipitation fields are simulated, to include a more realistic setup. The advection model calculates drop size specific wind drift on precipitation, which is a substantial difference to the PMA that returns one single wind drift value for the whole precipitation field. In section 4.2, the advection model is combined with the PMA to compare the obtained wind drift of the advection model to the wind drift obtained by the PMA.

4.1. Model Characteristics

The advection scheme simulates wind drift over an area of $350 \times 350 \text{ km}^2$ around the DWD radar in Boostedt. Only the horizontal drift due to wind and the gravity force that leads to the terminal velocity of droplets are considered. All droplet interactions, such as coalescence or evaporation are omitted to make

the model as simple as possible. It is further assumed that water droplets are horizontally drifted at wind speed, although the horizontal droplet speed and the wind speed gradually diverge in reality (Pedersen and Hasholt, 1995; Testik and Pei, 2017). However, these differences are small and should not have major consequences. The model is initialized with precipitation fields in mm h^{-1} at the boundary height of 3 km and simulates the horizontal displacement of water droplets while falling. The boundary height of 3 km was chosen to obtain as much fall time as possible, while ensuring that the water droplets are mainly in liquid phase. It is assumed that no ice or snow particles are present. The vertical terminal velocity is dependent on the droplet size and thus, a given rain field in mm h^{-1} must be transformed to a drop size distribution first. This is done according to Marshall and Palmer (1948):

$$N_D = N_0 e^{-\Lambda D} , \quad (4.1)$$

with the intercept $N_0 = 8 \cdot 10^3 \text{ mm}^{-1} \text{ m}^{-3}$ and the slope $\Lambda = 4.1 R^{-0.21}$, where R is the rainfall rate in mm h^{-1} . Only drop diameters between 0.5 mm and 5 mm with bin sizes of 0.5 mm are considered, resulting in a total of 10 drop size bins.

The terminal velocity is then calculated according to (Atlas et al., 1973):

$$v_t(h) = (9.65 - 10.3 \cdot e^{-0.6D}) \cdot \delta(h) , \text{ for } 0.109 \text{ mm} \geq D \geq 6 \text{ mm} , \quad (4.2)$$

with the height dependent factor $\delta(h)$ according to eq. (3.21). After initializing the model with a precipitation field in mm h^{-1} and calculating the drop size distribution, the model will then simulate the rainfall with predefined time steps. This simulation is implemented stepwise for each grid volume and for each drop size bin. All drops of a specific drop size bin D within a specific grid volume are subtracted from the original grid volume and added to the corresponding grid volumes after applying the horizontal and vertical displacement due to wind drift and vertical velocity (Figure 4.1). This procedure is then repeated for all grid volumes and drop size bins before the calculation of the

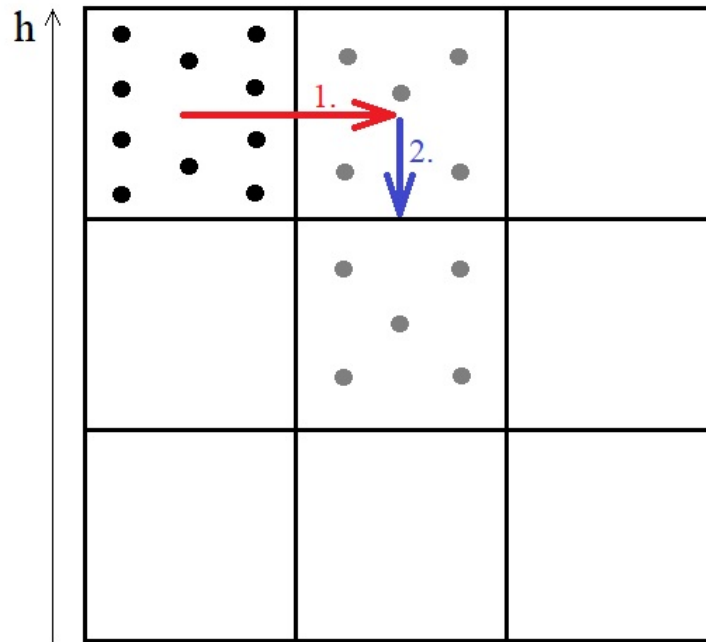


Figure 4.1: Implementation of horizontal displacement and vertical displacement of rain droplets. The red and blue arrow illustrate horizontal and vertical displacement respectively. Black dots illustrate rain drops before the displacement was applied, gray dots illustrate rain drops after the displacement.

next time step starts. The order of the grid volumes is important. There is no updraft considered in this model and thus, droplets can only move downwards. When starting from the highest grid volumes, some of the droplets are advected to grid volumes below. This means these droplets would be advected again within the same time step when processing the grid volumes from highest to lowest. To prevent this, the displacement is applied starting from the lowest grid volumes. The droplets are assumed to distribute equally over one grid volume. The horizontal displacement is applied first and simply calculated by multiplying the wind speed of the given wind profile at the current height with the length of one time step:

$$s_h = \vec{v}\Delta t , \quad (4.3)$$

where \vec{v} and Δt mean the wind speed in m s^{-1} and the length of one time step in s respectively. The vertical displacement within one time step is calculated analogously, by multiplying the terminal velocity from eq. (4.2) with the length of one time step. After the horizontal and vertical displacements within one time step were calculated, the droplets from the current drop size bin D and from the current grid volume are subtracted from the originating grid volume and added to the corresponding grid volumes after the displacement was applied. In case of displacements not matching the grid resolution, the droplets are distributed to the neighboring grid volumes according to the percentage of overlap. For example, with grid volumes of 1 m^3 , a vertical displacement of 0.75 m and no horizontal displacement, 25% of the droplets would be distributed to the originating grid volume, while 75% would be distributed to the grid volume directly below (Figure 4.2).

This scheme is a very simple advection based model, but the simplicity comes with small drawbacks. It is based on a forward Euler method: The terminal velocity and the horizontal displacement due to wind drift are calculated from the originating grid volume but are applied for the whole trajectory that a droplet is displaced within one time step. This means, any change in the terminal velocity or wind profile along this trajectory is ignored. This error can be minimized by choosing very small time steps so that the time until the environment is updated becomes very short. Also, the grid volumes should be small to minimize the truncation error: Due to the assumption that all droplets are always equally distributed within one grid volume, droplets could travel over unrealistic high distances when the grid volumes are too large. For example, at a terminal velocity of 10 m s^{-1} , a time step of 1 s and grid lengths of 500 m, the droplets fall 10 m within one time step. This means, at the first time step, 10/500 of all droplets within the first grid volume would fall into the second grid volume. As a result, for $N=2500$ original droplets, 50 droplets would be assigned to the second grid volume. Within the next time step, 10/500 of these 50 droplets would be assigned to the third grid volume. In

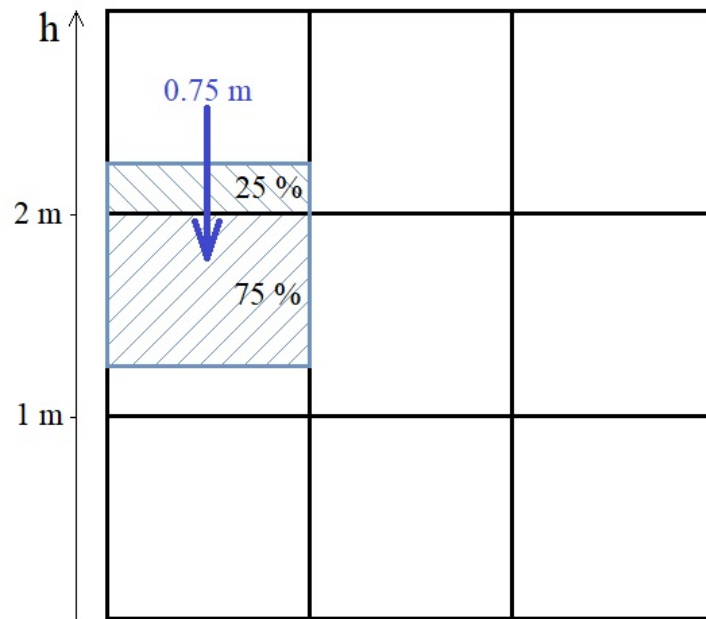


Figure 4.2: The percentage of overlap after the displacement of a grid volume. The blue box is the grid volume that was displaced downwards by 0.75 m. Hatching lines from bottom right to top left illustrate overlap with the top grid volume, Hatching lines from bottom left to top right illustrate overlap with the grid volume below.

this scenario, this equals to one droplet that traveled more than one grid box and thus over 500 m within two seconds. However, the share of the original droplets that are simulated to travel over such high distances is very low. Nevertheless, this error can be minimized by limiting the grid volume. Since both time step and grid length should be minimized, a grid length of 200 m and a time step of 20 s was chosen for this model. The grid length of 200 m equals the grid resolution used for the PMA in chapter 3. The time step of 20 s was chosen so that at terminal velocities of a magnitude at 10 m s^{-1} a droplet would travel one grid volume. Since terminal velocities rarely exceed 10 m s^{-1} , the Courant-Friedrichs-Lewy (CFL) condition is met:

$$\frac{v_t \Delta t}{\Delta x} \leq 1, \quad (4.4)$$

where v_t is the terminal velocity, $\Delta t=20$ s is the length of one time step and $\Delta x=200$ m is the grid resolution.

Synthetic Rain Fields

To show some of the characteristics of this advection model, a stationary and artificially created precipitation field is used to initialize the model. When artificially creating the initialization precipitation field a very smooth and regular initialization can be ensured so that it is easier to identify the basic characteristics of the model. The artificially created rain field spreads over the whole model area and has a rain fall rate with a \sin^2 -dependency in x - and y -direction:

$$R = 25 \cdot \sin(x/33 - 0.69)^2 \cdot \sin(y/33 - 0.26)^2 + 0.1 , \quad (4.5)$$

where x and y are Cartesian coordinates in m, ranging from 0 to the maximum of 350 km. By initializing the rain field this way, a maximum rain fall rate of 25.1 mm h^{-1} is assured and the rainfall rate never reaches zero. The sines are scaled so that exactly four precipitation maxima lie directly over Hamburg. Figure 4.3 shows this initialization rain field for the area of Hamburg. For better comparison with radar measurements, the rain fall rate was transformed to the drop size distribution (eq. (4.1)) and then to the reflectivity factor z in $\text{mm}^6 \text{ m}^{-3}$ according to Doviak and Zrnic (2006):

$$z = \sum_{i=0}^{41} N_i D_i^6 \Delta D_i , \quad (4.6)$$

where i iterates over the number of drop size bins and N_i and D_i are the corresponding number of droplets and drop diameter respectively. ΔD_i is the width of the drop size bin, which is 0.5 mm for all drop size bins in this work. The reflectivity factor z is then transformed to the relative reflectivity factor Z in units of dBZ according to eq. (3.9). A simulation using this rain

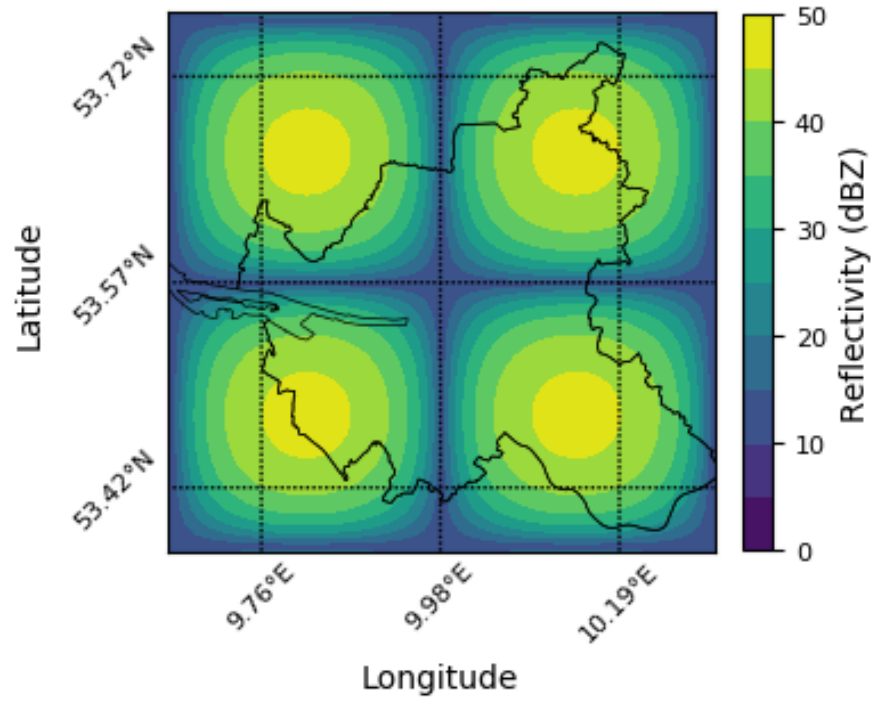


Figure 4.3: Artificially created and stationary precipitation field over Hamburg.

field to initialize the precipitation at the height of the top boundary (3 km) and with a time step of 20 s, a grid length of 200 m and a constant wind profile of southwesterly winds at 20 m s^{-1} is shown in Figure 4.4. A constant wind of 20 m s^{-1} is very high, but with strong winds the basic characteristics of the advection scheme are stronger pronounced and visible on a scale of a relatively big city like Hamburg. The rain field at 3 km is stationary for this simulation, which means that the boundary height is initialized again at each time step with the precipitation field created from eq. (4.5) so that the precipitation

field at 3 km is constant over the whole simulation. The precipitation maxima of the initialized precipitation fields arrive first at ground level (second picture on the right hand side), whereas the edge arrives some time steps later (third picture on the right hand side). This is due to the fact that smaller droplets have a lower terminal velocity compared to bigger droplets. The precipitation maxima consist of more bigger droplets, which arrive at the ground first. Also, the whole precipitation pattern is moved to the northeast, compared to the initial precipitation field as seen in Figure 4.3. This is due to the southwesterly wind profile, which causes all droplets to be drifted to the northeast. But the pattern is not only shifted towards northeasterly directions as a whole, the four precipitation fields are also smoothed and skewed to the northeast. The skewness becomes stronger, the lower the height is and the longer the simulation was run. This feature can be explained by the difference in terminal velocity between smaller and bigger droplets too. As smaller droplets have a lower terminal velocity, the fall time until they reach the ground is longer and thus smaller droplets are exposed over a longer period of time to the horizontal drift. That's why, the precipitation maxima are shifted only a little to the northeast, whereas the edges of the precipitation fields are shifted more strongly, which results in the skewed pattern. This effect can be considered as a spatial drop sorting. The bigger droplets stay in close range to the precipitation maxima, whereas the skewed edges of the precipitation patterns contain only small droplets. In summary, the simulation shows three characteristics: Bigger droplets reach lower heights first, the whole precipitation pattern is shifted into the wind direction and the precipitation fields become skewed while falling, which is equal to a spatial drop sorting. Since these characteristics are to be expected when modeling drop size dependent drift of water droplets, the model simulates the basic processes correctly.

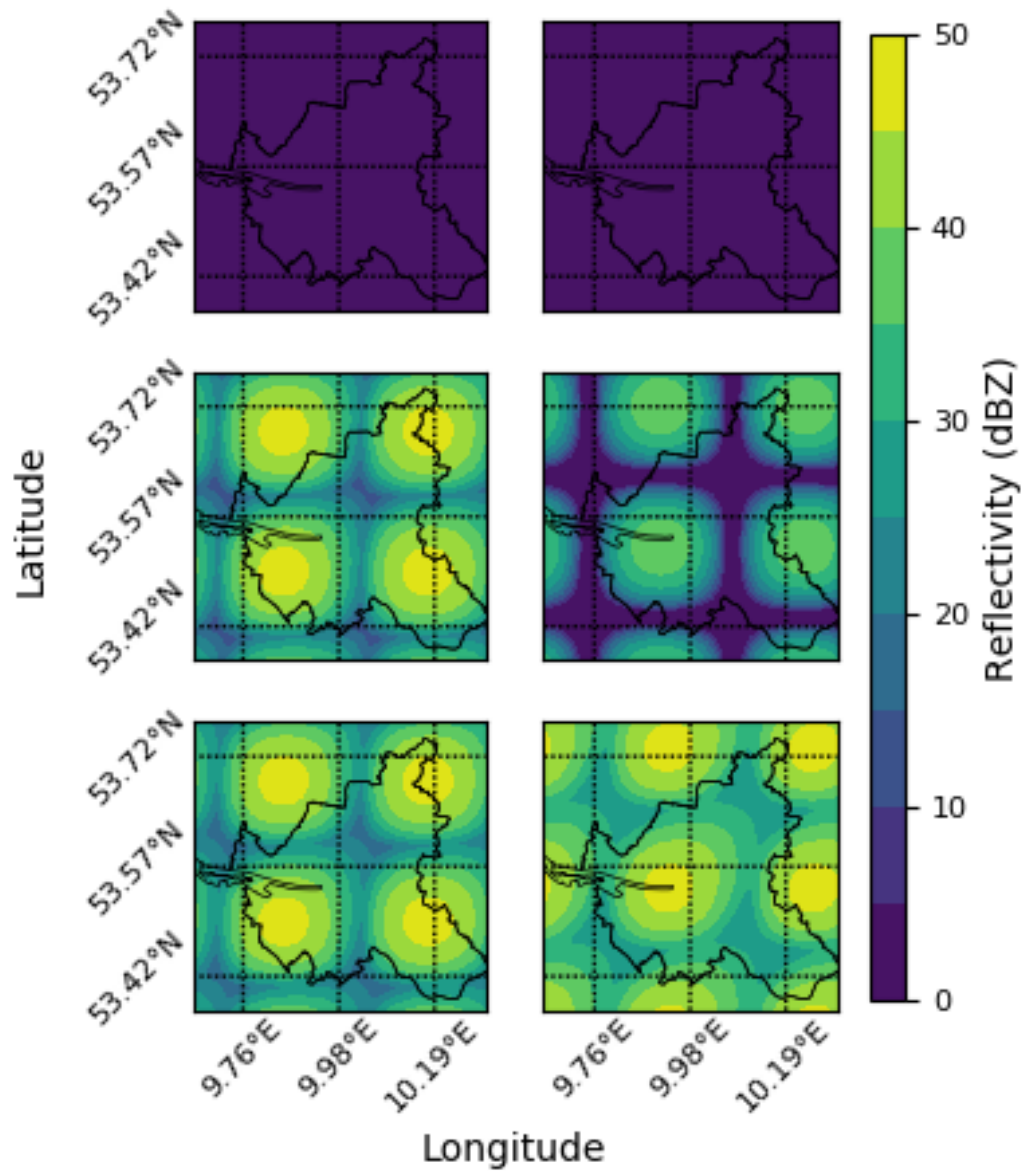


Figure 4.4: Simulation of precipitation under the influence of wind drift. Left column at 2 km height. Right column at ground level. First row at time step of 0 s, second row at 300 s, third row at 1000 s.

Measured Rain Fields

In reality, precipitation fields are rarely stationary and certainly almost never sinusoidal. To create a more realistic setup, the model is initialized with measurements from a radar. A CAPPI at 3 km height was created from the volume scan at the June 7th, 2016, 16:20 UTC of the DWD radar in Boostedt. Furthermore, the boundary at 3 km height is updated at each time step with a new precipitation field to realize a non-stationary boundary condition. The temporal resolution of the model (20 s) is higher than the temporal resolution of the DWD radar scan (5 min) though. That's why the temporal resolution of the DWD radar is increased by linear interpolation between the CAPPIs of two consecutive scans:

$$R = R_B \frac{\Delta t_B}{\Delta t_A + \Delta t_B} + R_A \frac{\Delta t_A}{\Delta t_A + \Delta t_B}, \quad (4.7)$$

with R_B and R_A being the reflectivity of the scan before and after the corresponding model time stamp and Δt_B and Δt_A being the corresponding time differences to the model time stamp in seconds. This interpolation is done for each grid box of the model domain individually so that at each model time step a complete precipitation field at the boundary height of 3 km is available. A simulation initialized with these linear interpolated precipitation fields is shown in Figure 4.5. When looking at the left side of Figure 4.5, one can see small changes within the precipitation fields. The precipitation field in the southwest corner for example shrinks over time, whereas the northeasterly precipitation field just changes its shape a little. The small reflectivity echo in the southeast of Hamburg is only visible at the first time step and diminishes completely afterwards. These changes result directly out of the updated CAPPIs at 3 km height from the DWD radar volume scan. After 300 s (second row), the northeasterly and southwesterly precipitation fields are already visible at ground level (right column). Both have been shifted a little to the northeast due to the wind drift of the southwesterly wind profile. Furthermore, both

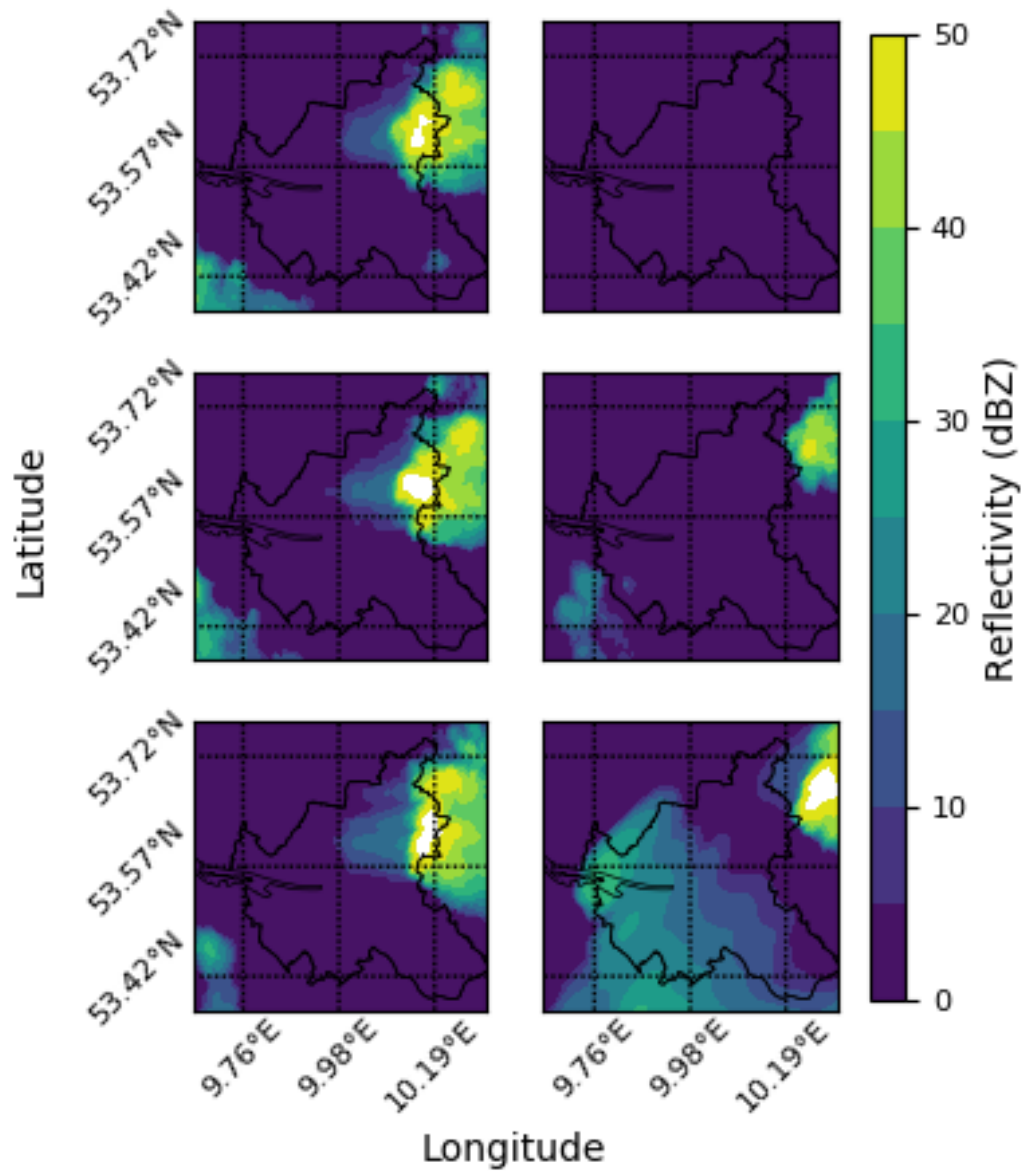


Figure 4.5: Same as Figure 4.4, but with a non-stationary initialization with CAPPs at 3 km height. The left column is at initialization height of 3 km, the right column at ground level.

precipitation fields are a little smaller in extension because at 300 s only the big droplets have arrived at the ground. At 1000 s, most droplets have arrived and a widespread precipitation field is visible over large parts of the south and center of Hamburg. This precipitation field was advected from the southwest, outside of the Hamburg area. It consists of small to medium droplets, which explains the far drift distances. Thus, the basic model characteristics remain the same when using a non-stationary initialization with radar CAPPIs at the boundary height of 3 km: Bigger droplets reach the lower heights first, all droplets are drifted into wind direction and small droplets are drifted further. The resulting precipitation fields will never stay constant however because the input CAPPIs at boundary height are updated with new measurements at every time step.

4.2. Combination with PMA

By now, two fundamentally different methods to calculate wind drift have been presented. One takes a theoretical approach to model the falling of water droplets, the other one compares measured images of precipitation field to find the drift between two heights. It would be interesting to know how much the absolute wind drift calculated by these methods differ. That's why the following last section focuses on comparing the two methods.

To allow for a comparison, the advection scheme is dependent on a correct input wind profile. There are no volume-covering wind measurements over the radar volume available. To create a realistic wind profile for the advection scheme, there are three options available:

1. Sounding profile
2. Backwards approach
3. Using PMA relative drift profile

The first option is to simply feed the sounding wind profile into the advection scheme. This option is the easiest to implement but there is an error linked

to this approach as the sounding profile is not valid for the whole radar area but rather only along the soundings trajectory. The backwards approach finds the wind profile by trying different wind profiles until the precipitation fields of the model are similar to the CAPPs created by the PMA. However, this approach focuses on matching the precipitation fields which does not guarantee a realistic input wind profile. Also, the tuning of the model with CAPPs from the PMA makes a comparison impossible because the precipitation fields and the wind drift will always be very similar. The third option to obtain a realistic wind profile is by using the information from the PMA about the relative drift between two heights. When assuming the precipitation fields are drifted at wind speed, the wind vector \vec{v} at this height could be calculated using the relative drift \vec{d}_r together with the fall time t of the precipitation:

$$\vec{v} = \frac{\vec{d}_r}{t_f}. \quad (4.8)$$

Unfortunately, the fall time t_f is unknown. The fall time t_D of a specific drop size can easily be calculated using the terminal velocity from eq. (3.20). A precipitation field consists of droplets at many different sizes though. To obtain a representative drop diameter, again the median volume diameter D_0 is calculated (eq. (3.15) and eq. (3.19)). Solving eq. (3.20) for the median volume diameter D_0 gives a representative fall velocity from which a representative fall time t_f is calculated. Together with the relative drift from the linear drift profile, this yields the wind speed according to eq. (4.8). However, there is a caveat connected to this approach, too. When using the original grid resolution of the PMA, there are only very few drift values possible between to neighbored heights. Since two neighbored heights are only 200 m apart, the relative drift calculated by the PMA almost always returns values of 0 m or 200 m. On rare occasions, also relative drift values of 400 m have been calculated. This means that a wind profile calculated out of the PMA's relative drift at the original resolution basically consists of 2-3 big wind speed

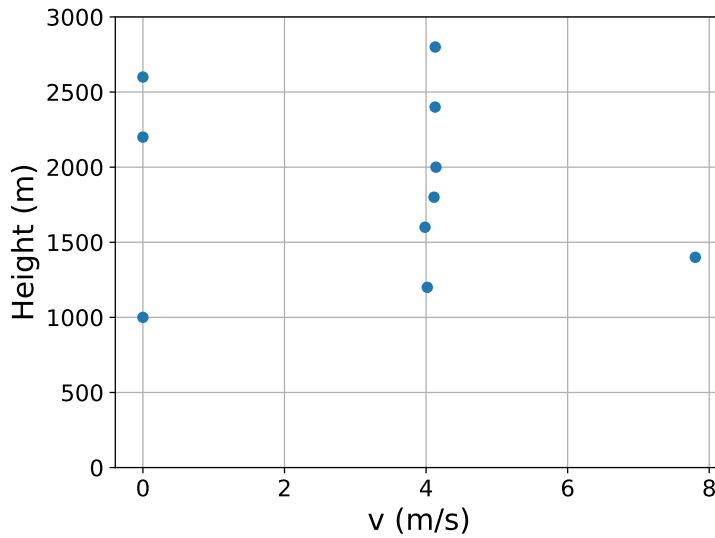


Figure 4.6: Wind speed profile obtained by using the PMA drift and a median volume diameter for the 07.06.2016, 16:20 UTC.

steps (Figure 4.6) and otherwise only very small variations due to small differences in the median volume diameter. In Figure 4.6 for example, a relative drift of 0 was calculated three times, resulting in the three dots at a wind speed of 0. A relative drift of 200 m was calculated six times, corresponding to the six blue dots near 4 m s^{-1} . Only once there was a relative drift of 400 m, which leads to the single blue dot at around 8 m s^{-1} . This clearly illustrates the low wind speed resolution when obtaining the wind profile from the PMA relative drift profiles. To increase the amount of possible wind speed values, the fraction of horizontal to vertical resolution must be increased so that more relative drift steps are possible. The horizontal resolution cannot be further increased since the resolution of 200 m is already extremely high considering the resolution of the DWD radar scans of 250 m to 1 km. Thus, the vertical resolution must be coarsened to make more relative drift steps possible. To guarantee a sufficient amount of relative drift steps, the vertical resolution must be coarsened to 1 km or more. Although this solves the described problem, a vertical resolution of 1 km is too low to yield physically meaningful results.

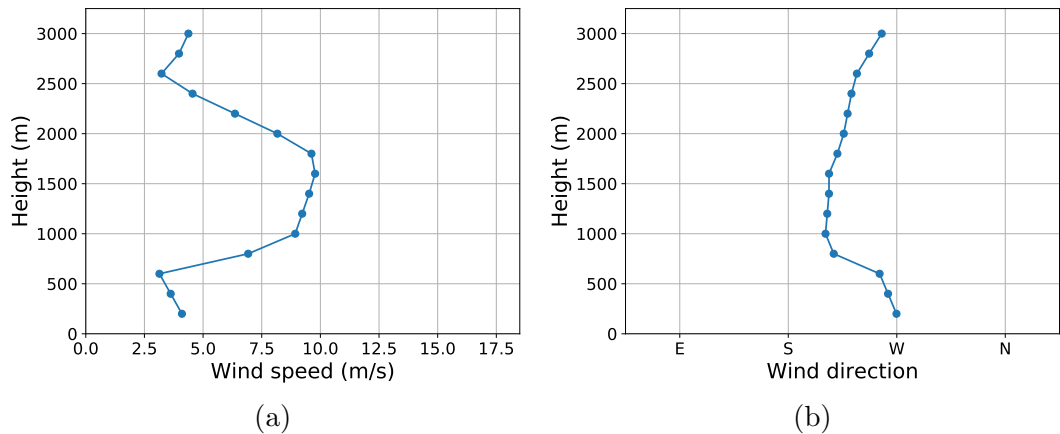


Figure 4.7: Wind profile measured by the Schleswig-sounding on 07.06.2016 at 12 UTC. a) Wind speed, b) Wind direction.

Within 1 km drastic changes in the wind profile or the precipitation are possible, which make a vertical resolution of 1 km futile.

Since option 2 and 3 to retrieve the wind profile yield unsatisfactory results, the wind profile of the advection scheme will be predefined by the soundings (option 1, Figure 4.7). The only caveat of this wind profile is the limited areal representativity. The induced error should be very small when the wind profile is rather constant over the radars measurement area. Soundings do not measure the height directly but the air pressure instead. The air pressure was transformed into the height by calculating the thickness h_1^2 of the layer between measurements at two neighbored heights Z_1 and Z_2 according to the hypsometric equation (Wallace and Hobbs, 2006):

$$h_1^2 = Z_2 - Z_1 = \frac{R_d \bar{T}_v}{g} \ln\left(\frac{p_1}{p_2}\right), \quad (4.9)$$

where $R_d=287 \text{ J K}^{-1} \text{ kg}^{-1}$ is the gas constant for dry air, \bar{T}_v is the mean virtual temperature within the layer between the heights Z_1 and Z_2 , p_1 and p_2 are the pressure levels at height Z_1 and Z_2 respectively and $g=9.81 \text{ m s}^{-2}$ is the

acceleration due to gravity.

Starting from the ground, the stepwise summation of the thickness between all measurements levels until level n results in the height at level n :

$$h_n = \sum_{i=1}^{n-1} h_i^{i+1} . \quad (4.10)$$

As long as the real wind profile is not changing much within the measurement area, the sounding wind profile is a realistic approximation to use for modeling the wind drift. This wind profile in combination with the CAPPIs from the DWD radar represent a realistic setup for the advection scheme to model the influence of wind drift on precipitation. Such a simulation with a stationary wind field defined by the sounding wind profile is shown in Figure 4.8. This run was initialized at a boundary height of 3 km with the 3 km-CAPPI of the DWD radar. The boundary height was updated in a non-stationary manner (see previous section 4.1), also with 3 km-CAPPIs from the DWD radar. The model simulation runs over a time of 25 minutes to guarantee that even the smallest droplets have reached the ground. When comparing Figure 4.8 to Figure 4.5, a strong similarity becomes apparent. This is a result of the sounding measurements showing similar wind directions as the wind profile for the simulation of Figure 4.5. Both wind profiles mainly consist of southwesterly winds. As a result, in both simulations the precipitation is drifted to the north-east. In Figure 4.8 however, the precipitation is not drifted nearly as far as in Figure 4.5 due to the much lower wind speeds of 3 m s^{-1} to 10 m s^{-1} compared to the 20 m s^{-1} wind speed used in Figure 4.5. The advection scheme simulates the fall trajectory of all drops. By combining these droplets to a reflectivity according to eq. (4.6), it is simulated what a radar would theoretically measure at these heights. By using the simulated reflectivity images of two neighbored heights, it is possible to apply the same template matching algorithm used by the PMA in chapter 3. Following the same procedure as in section 3.2, a profile of relative drift is created by calculating the relative drift

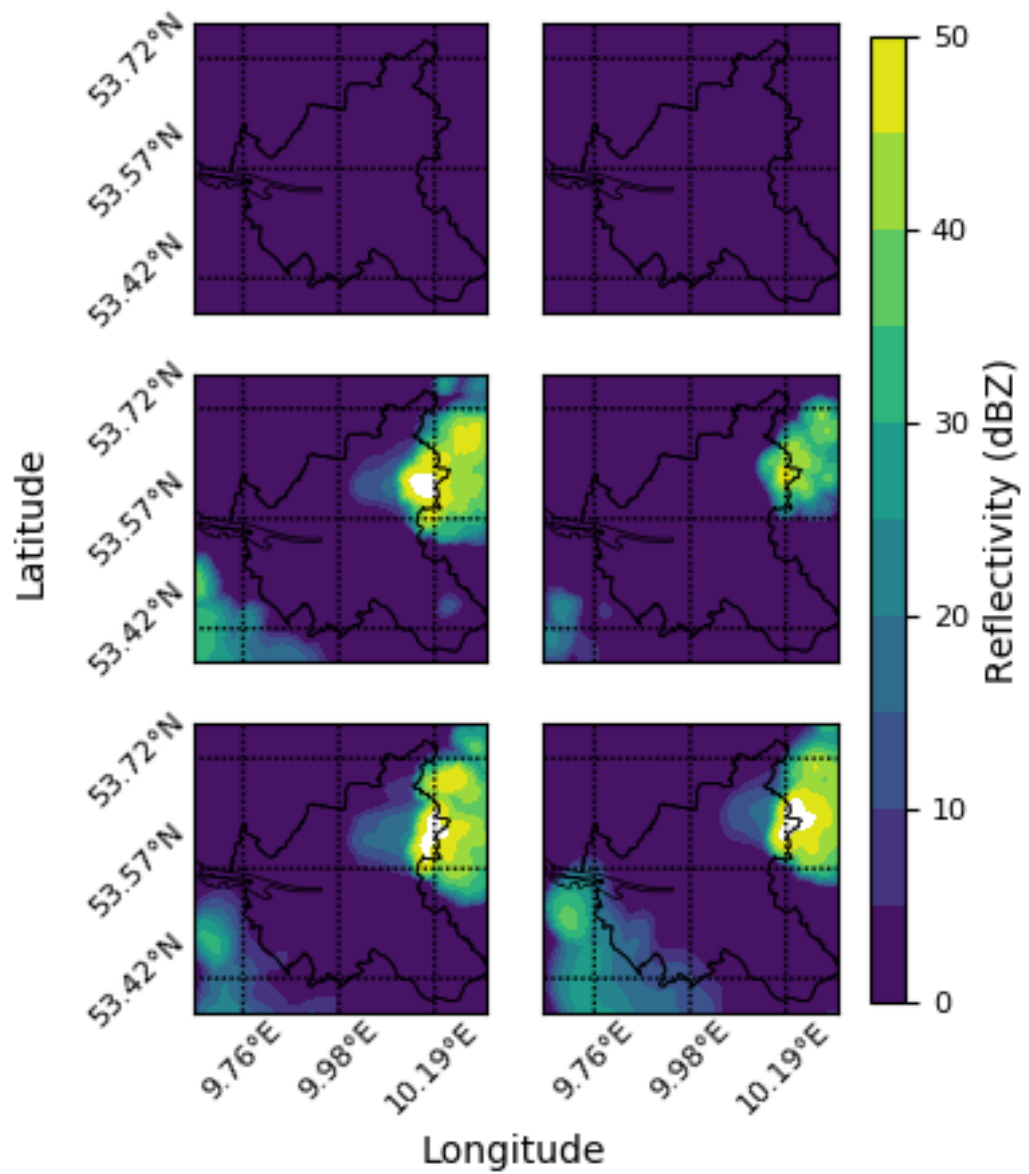


Figure 4.8: Same as Figure 4.5, but initialized with the sounding wind profile seen in Figure 4.7. The left column is at height of 2 km, the right column at ground level.

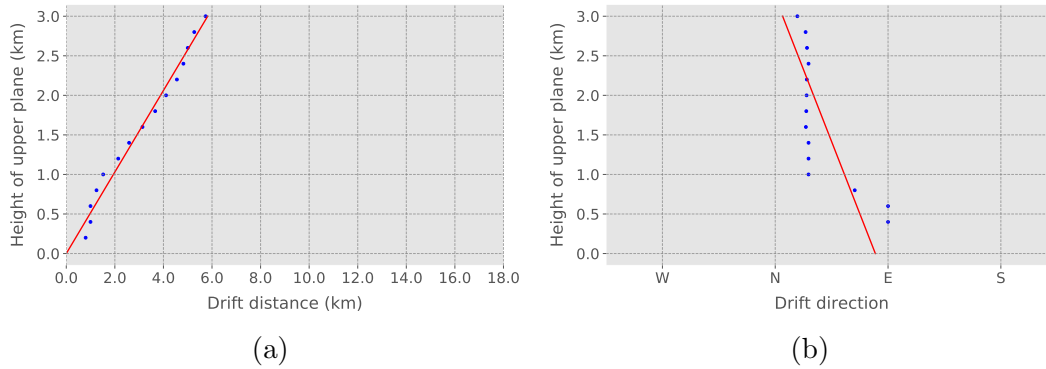


Figure 4.9: Simulated profiles of relative drift for the precipitation event a). On the left-hand side: Profile of relative drift distance. On the right-hand side: Profile of relative drift direction. Blue dots are drift values as calculated by the template matching algorithm for the simulated reflectivity fields. A linear least-squared fit is visualized as the red line. An offset was added so that the relative drift distance of the linear fit at ground equals zero.

at one time step for all heights of the grid relative to the ground using the template matching algorithm (Figure 4.9). To obtain the absolute wind drift, the traveled distance of the original precipitation field is added to the relative drift according to eq. (3.12) (Table 4.1). The travel speed and the travel distance of the precipitation is identical to the travel speed and distance from part 3.2.2 (Table 3.3) for all events. This is because the advection scheme is initialized with the same radar measurements at 3 km height as used in part 3.2.2 for calculating the travel speed.

On average, the advection scheme simulates a relative drift of 3.6 km and an absolute wind drift of 7.2 km between 3 km and the ground for the six precipitation events (Table 4.1). This means the advection scheme calculates on average greater wind drift values compared to the wind drift calculated by the PMA in section 3.2 (2.75 km relative drift, 3.8 km absolute drift, Table 3.2). In case of event b) and d), the advection scheme shows more than twice the drifted distance compared to the PMA. There are several possible explanations

Table 4.1: Wind drift between 3 km and ground according to the advection scheme after a simulation time of 25 minutes.

Event	Rel. distance	Abs. distance	Rel. direction	Abs. direction
a)	5.8 km	6.7 km	7°	45°
b)	3.6 km	7.1 km	305°	313°
c)	3.1 km	5.4 km	303°	345°
d)	2.4 km	2.1 km	180°	124°
e)	3.7 km	13.8 km	336°	25°
f)	2.8 km	7.8 km	131°	12°

Table 4.2: Wind drift between 3 km and ground, where only drop bins larger than 1 mm have been included.

Event	Rel. distance	Abs. distance	Rel. direction	Abs. direction
a)	2.0 km	2.4 km	302°	89°
b)	2.2 km	1.4 km	136°	330°
c)	2.0 km	1.8 km	210°	5°
d)	1.1 km	1.0 km	228°	65°
e)	3.6 km	13.5 km	331°	24°
f)	6.1 km	3.4 km	177°	358°

for the high wind drift values. The first possibility could be the missing droplet interactions within the model. When no droplet interactions are simulated, the small droplets within the 0.5 mm bin stay small over the whole fall distance and thus are drifted very far. This could deform the precipitation field a lot and lead to high drift values found by the template matching algorithm. To check this theory, the same simulation was run using only drop bins larger than 1 mm (Table 4.2). Except for event e) where very high winds have been measured (Table 2.2), the wind drift values calculated are much lower with an average absolute wind drift of 3.9 km, which means that the theory of an extreme influence of small droplets on the template matching algorithm proves to be correct and explains the high wind drift values. When comparing

the drift direction another interesting feature becomes apparent. For most events, the relative drift and the absolute drift point into similar directions when all drop bins are included (Table 4.1), whereas they point into opposite directions for all events when the smallest drop bins are excluded (Table 4.2). The PMA in part 3.2.2 calculates relative and absolute drift of opposite direction too (Table 3.2). An absolute drift direction opposite compared to the relative direction is to be expected because the wind speed is usually greater at higher altitudes. When assuming precipitation fields are drifted at wind speed, this would result in precipitation fields at high altitudes being drifted further than the horizontal drift that droplets experience while falling to the ground (Figure 3.6b). In this case, the relative drift between 3 km and ground is of opposite direction compared to the absolute drift direction and thus, the relative drift direction as calculated by the PMA and by the advection scheme where the small drop bins have been excluded seem to be more realistic. The absolute and relative drift simulated by the advection scheme with all drop bins included point into the same direction. This means that the advection scheme horizontally drifts the precipitation further while falling than the original precipitation field at 3 km height has moved during the fall time. This further strengthens the impression that the influence of smallest droplets on the simulation is too large.

Chapter 5

Conclusion and Outlook

Most of the volume measured by a radar is at considerable height above ground. At the same time, most applications are interested in precipitation at ground level. There are several sources of error when projecting radar derived precipitation measurements to the ground. One of these errors is the wind induced horizontal displacement: The wind drift. Two different methods have been introduced to determine the impact of wind drift on precipitation. The underlying weather radar data consists of the precipitation and volume scan of the DWD radar in Boostedt. This radar is capable of producing polarimetric precipitation scans at 11 different elevation angles between 0.5° and 25° at horizontal resolutions of 250 m to 1 km and with ranges up to 180 km. The first method to calculate the effect of wind drift is solely based on the DWD radar data. This data is interpolated to a three dimensional Cartesian grid at 200 m vertical and horizontal resolution using Linear Barycentric Interpolation. Planes of constant altitude (CAPPIs) are taken from this grid to visualize precipitation at a constant height. By applying a template matching approach, CAPPIs of different heights are matched to find the shift at which the normalized cross-correlation between these two CAPPIs is at its maximum. This shift is the relative drift between precipitation fields at two different heights at a single time. To obtain information about the drift relative to the ground, the drift of several heights relative to a base CAPPI is calculated and linearly extrapolated to the ground. The absolute wind drift that a precipitation field

would experience while falling to the ground is then calculated by adding the traveled distance of the original precipitation field to the relative drift. The travel distance of the original is found by calculating the travel speed and the fall time of the precipitation field. The chosen fall time is a representative fall time that is obtained from the median volume drop diameter. The travel speed is found by matching two successive CAPPIs of the same height using the template matching algorithm. The whole procedure to find wind drift by applying a template matching approach on the CAPPIs of the DWD radar data is called Precipitation Matching Algorithm (PMA) in this study.

The second method to determine the impact of wind drift is based on a simple advection scheme that simulates the drop size dependent trajectory of rain drops under the effect of wind drift on a Cartesian grid with 200 m horizontal and vertical resolution. 10 drop size bins from 0.5 mm to 5 mm are included. No droplet interactions such as coalescence or evaporation are considered. It is assumed that the droplets are horizontally drifted at wind speed. The model is initialized with a wind profile from the sounding measurements of Schleswig at the closest time and updated at a boundary height of 3 km with CAPPIs from the DWD radar.

Both methods are applied to six different precipitation events in June, 2016. These events are characterized as heavy precipitation events, where large portions of the DWD radars range are covered with heavy rain. The wind profiles at these events are rather constant within the free atmosphere according to the soundings of Schleswig. The advection scheme calculates wind drift values seemingly too high. The most likely reason for this seems to be an overestimation of the influence of small droplets due to missing droplet interactions. When ignoring the smallest drops, more realistic wind drift values are found. With the advection scheme and the PMA at the hand, two methods have been presented that allow an answer on the leading question:

What is the impact of wind drift on radar-derived rainfall estimates?

It is found that the linear extrapolation to the ground of the wind drift cal-

culated by the PMA yields absolute wind drift distances of 3.8 km on average between 3 km height and ground level, ranging from 1 km (event d)) to 7.9 km (event e)). According to the advection scheme, wind drift values between 3 km height and the ground of 7.2 km occurred on average, ranging from 2.1 km (event d)) to 13.8 km (event e)) for the six precipitation events. Event d) was associated with the weakest winds of 0.88 m s^{-1} measured at the Wettermast Hamburg at 280 m height. Event e) was associated with the strongest winds of 19.02 m s^{-1} . The wind drift distances calculated by the advection scheme are considered too high due to the overestimation of the influence of small droplets. The large range of the wind drift values shows that the actual wind drift is strongly dependent on the wind profile. The average absolute wind drift of 3.8 km and 7.2 km between 3 km height and the ground is slightly lower than the wind drift found by other studies. Harrold et al. (1974) for example found wind drift between 1 km and 2 km already for precipitation falling from only 500 m to the ground. Lauri et al. (2012) suggests horizontal displacements on the order of tens of kilometers for liquid precipitation at ranges of 100-250 km to the radar site and with low elevation angles of 0.3° . The deviations to the wind drift found in this study could be a consequence of a difference in the wind profile, especially since the measured wind at the Wettermast Hamburg was below 7 m s^{-1} for all events except event e).

So far, there is no evaluation of the presented methods to calculate wind drift. Both methods calculate wind drift values similar but slightly lower than the wind drift found by other studies. Also, the PMA proves to provide very stable results as shown by the small standard deviation of the relative drift profiles (Part 3.2.3). As a result, there should be some confidence that these methods provide realistic results and could be used to correct weather radar measurements with wind drift. Although both methods will not provide perfectly accurate results, it is expected that this correction would lead to better results than simply projecting the precipitation to the ground without any horizontal advection.

Outlook

There are several possible ways to improve the applied methods. The advection scheme for example ignores all droplet interactions and simply calculates the drop size dependent trajectory of all droplets within the precipitation field. A more realistic setup could be created if effects such as coalescence, partitioning or evaporation are included. This would decrease the error due to the overestimation of the smallest droplets because the smallest droplets are unlikely to survive until reaching the ground in reality. Furthermore, the reflectivity measurements of the radar are transformed to a drop size distribution according to the Z-R relation of Marshall and Palmer (1948). This is a large error source because the Z-R relations vary heavily in reality. By classification of the precipitation into stratiform or convective precipitation a better fitting Z-R relation could be used to get information about the drop size distribution.

The first method linearly extrapolates the relative drift profile to the ground. However, the wind profile generally observed within the surface layer is of logarithmic shape (Holton and Hakim, 2012). The method could be improved by extrapolating the relative drift profile to the ground using a logarithmic wind profile within the surface layer. This logarithmic wind profile could be calculated for example by fitting a logarithmic function to wind measurements at the ground. Even better would be measurements throughout the surface layer so that no extrapolation is needed. However, wind measurements throughout the surface layer are rarely available.

Finally, an evaluation of both methods with measured ground data is missing. Although both methods show realistic values for wind drift at a magnitude similar to wind drift found by other studies, systematic errors cannot be ruled out. A detailed evaluation with measured precipitation at the ground and measured wind profiles throughout the atmosphere is needed to confirm that both methods are providing valid results. A continued study focusing on the evaluation of these methods is therefore suggested for verification.

Acknowledgement

To all friends and colleagues, advisors and family involved in my work in any way: Thank you so much! I owe you a lot.

First of all, I would like to thank the Deutscher Wetterdienst for providing me with all necessary data. Their radar network data was highly useful to me and is a great accomplishment for the meteorological community in my opinion.

Furthermore, I'd like to thank Andreas Kuchenbecker from Hamburg Wasser for helping me to choose the most interesting precipitation events for my analysis.

I would also like to thank my advisors Prof. Dr. Felix Ament and especially Dr. Marco Clemens. During weekly discussions, you would consistently provide me with interesting insights and inspirations, while encouraging me to make my own decisions regarding the research of this thesis. Your door was always open for me, whenever I had questions or ran into problems.

I am lucky to have plenty of colleagues and friends who have been a great help in many situations. Yann Büchau and Simon Michel: As office colleagues and friends, you have always been available for countless interesting discussions on programming, research and writing issues, or on the nice view over Hamburg from our office window. Furthermore I'd especially like to mention Tobias Finn. I enjoyed our regular lunches, where we always dove right into discussions about my work, very rarely about yours. I appreciate that very much.

Finally, I want to express my deepest gratitude to my family and to my fiancée, Annabelle Köcher for your unconditional support. This work would have simply not been possible without you. Thank you.

Bibliography

- Atlas, D., Srivastava, R. and Sekhon, R. S. (1973). Doppler radar characteristics of precipitation at vertical incidence, *Reviews of Geophysics* **11**(1): 1–35.
- Austin, P. M. (1987). Relation between measured radar reflectivity and surface rainfall, *Monthly Weather Review* **115**(5): 1053–1070.
- Barber, C. B., Dobkin, D. P. and Huhdanpaa, H. (2013). Qhull: Quickhull algorithm for computing the convex hull, *Astrophysics Source Code Library*.
- Brümmer, B., Lange, I. and Konow, H. (2012). Atmospheric boundary layer measurements at the 280 m high hamburg weather mast 1995–2011: mean annual and diurnal cycles, *Meteorologische Zeitschrift* **21**(4): 319–335.
- Collier, C. (1999). The impact of wind drift on the utility of very high spatial resolution radar data over urban areas, *Physics and Chemistry of the Earth, Part B: Hydrology, Oceans and Atmosphere* **24**(8): 889–893.
- Deutscher Wetterdienst (n.d.). https://www.dwd.de/DE/forschung/atmosphaerenbeob/weterradar/weterradar_node.html. [Online; accessed: 2018-08-02].
- Doviak, R. J. and Zrnic, D. S. (2006). *Doppler radar and weather observations*, Courier Corporation.
- Etling, D. (2008). *Theoretische Meteorologie: Eine Einführung*, Springer-Verlag.
- Harrold, T., English, E. and Nicholass, C. (1974). The accuracy of radar-

- derived rainfall measurements in hilly terrain, *Quarterly Journal of the Royal Meteorological Society* **100**(425): 331–350.
- Helmert, K., Tracksdorf, P., Steinert, J., Werner, M., Frech, M., Rathmann, N., Hengstebeck, T., Mott, M., Schumann, S. and Mammen, T. (2014). Dwd's new radar network and post-processing algorithm chain, *8th Europ. Conf. on Radar in Meteorology and Hydrology, Garmisch-Partenkirchen*, pp. 1–6.
- Hoffmann, P., Merker, C., Lengfeld, K. and Ament, F. (2018). The hamburg tornado (7 june 2016) from the perspective of low-cost high-resolution radar data and weather forecast model, *Atmospheric Research* **211**: 1–11.
- Holton, J. R. and Hakim, G. J. (2012). *An introduction to dynamic meteorology*, Vol. 88, Academic press.
- Jones, E., Oliphant, T., Peterson, P. et al. (2001). SciPy: Open source scientific tools for Python, <http://www.scipy.org/>. [Online; accessed: 2018-07-03].
- Karney, C. F. (2011). Transverse mercator with an accuracy of a few nanometers, *Journal of Geodesy* **85**(8): 475–485.
- Lauri, T., Koistinen, J. and Moisseev, D. (2012). Advection-based adjustment of radar measurements, *Monthly Weather Review* **140**(3): 1014–1022.
- Lewis, J. (1995). Fast normalized cross correlation, *Industrial Light and Magic* .
- Marshall, J., Hitschfeld, W. and Gunn, K. (1955). Advances in radar weather, *Advances in geophysics*, Vol. 2, Elsevier, pp. 1–56.
- Marshall, J. S. and Palmer, W. M. K. (1948). The distribution of raindrops with size, *Journal of meteorology* **5**(4): 165–166.
- METEK GmbH (2009). *MRR Physical Basics*.
- Mittermaier, M. P., Hogan, R. J. and Illingworth, A. J. (2004). Using mesoscale model winds for correcting wind-drift errors in radar estimates of surface rainfall, *Quarterly Journal of the Royal Meteorological Society: A journal*

- of the atmospheric sciences, applied meteorology and physical oceanography* **130**(601): 2105–2123.
- o'Rourke, J. (1998). *Computational geometry in C*, Cambridge university press.
- Pedersen, H. S. and Hasholt, B. (1995). Influence of wind speed on rainsplash erosion, *Catena* **24**(1): 39–54.
- Preparata, F. P. and Shamos, M. I. (2012). *Computational geometry: An introduction*, Springer Science & Business Media.
- Sandford, C. (2015). Correcting for wind drift in high resolution radar rainfall products: A feasibility study, *Journal of Hydrology* **531**: 284–295.
- Sandford, C. (n.d.). A wind drift correction for radar rainfall products.
- Testik, F. Y. and Pei, B. (2017). Wind effects on the shape of raindrop size distribution, *Journal of Hydrometeorology* **18**(5): 1285–1303.
- University of Wyoming (n.d.). <http://weather.uwyo.edu/upperair/sounding.html>. [Online; accessed: 2018-07-10].
- Vince, J. (2017). *Mathematics for computer graphics*, Springer.
- Wallace, J. M. and Hobbs, P. V. (2006). *Atmospheric science: an introductory survey*, Vol. 92, Elsevier.
- Warmerdam, F. (2008). The geospatial data abstraction library, *Open source approaches in spatial data handling*, Springer, pp. 87–104.
- Werner, M. (2014). A new radar data post-processing quality control workflow for the dwd weather radar network, *Proc. 8th Europ. Conf. On Radar in Meteor. and Hydrol., Garmisch-Partenkirchen, Germany*.

Appendix A

Plots for all Precipitation Events

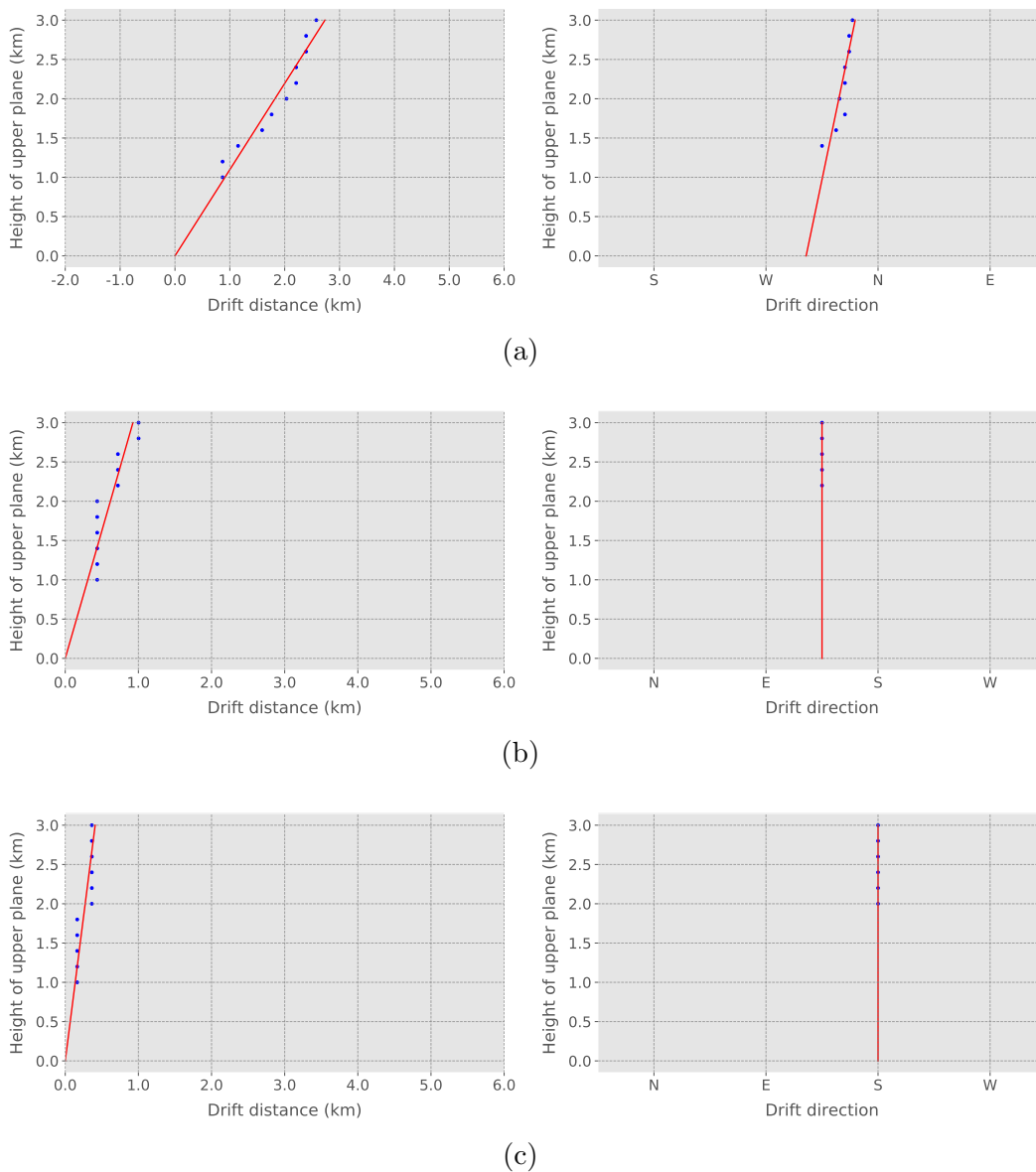
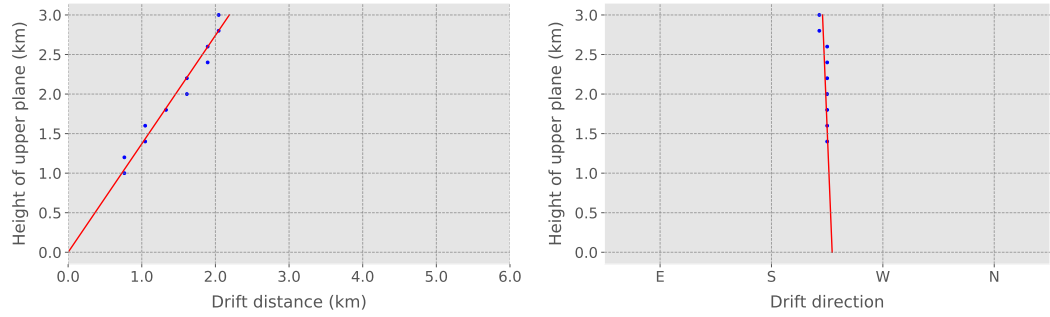
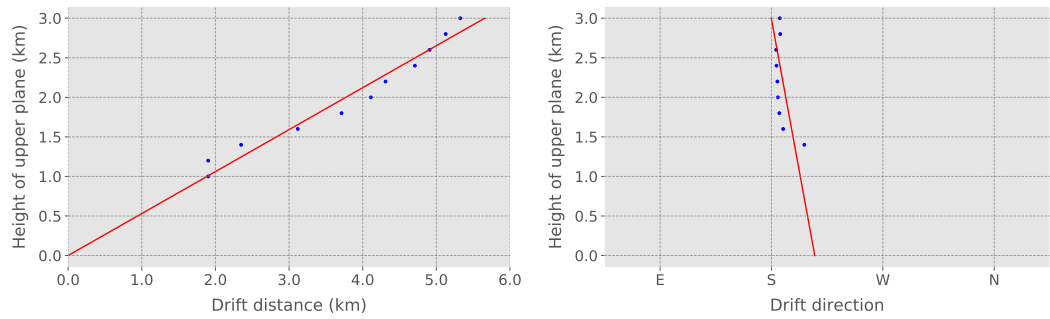


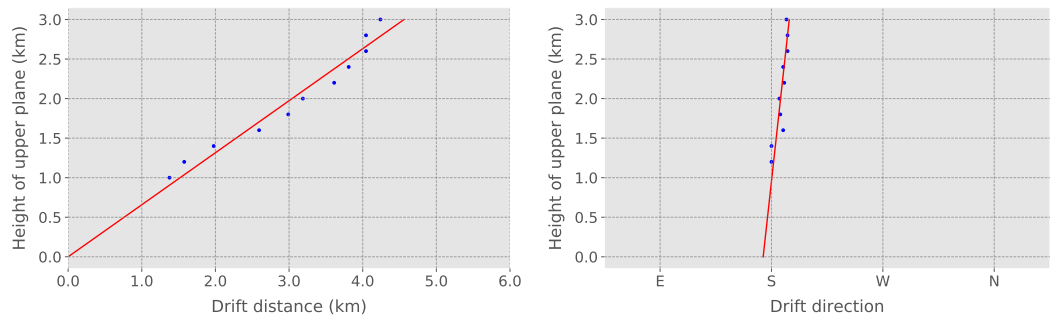
Figure A.1: Profiles of relative drift for the precipitation events a), b) and c). On the left-hand side: Profiles of relative drift distance. On the right-hand side: Profiles of relative drift direction. Blue dots are drift values as calculated by the template matching algorithm. A linear least-squared fit is visualized as the red line. An offset was added so that the drift at ground level equals zero.



(d)



(e)



(f)

Figure A.2: Same as Figure A.1, but for the precipitation events d) to f).

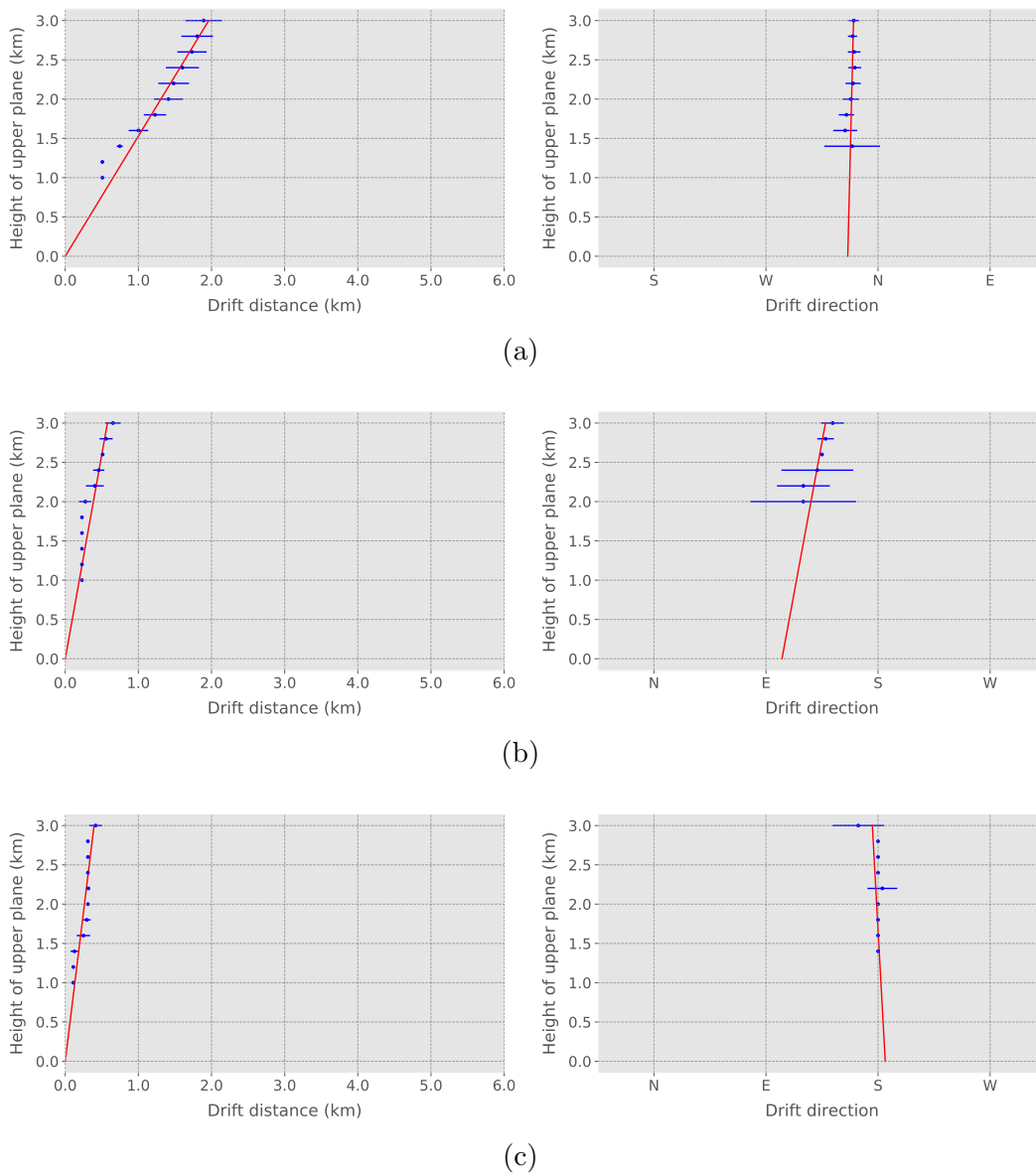
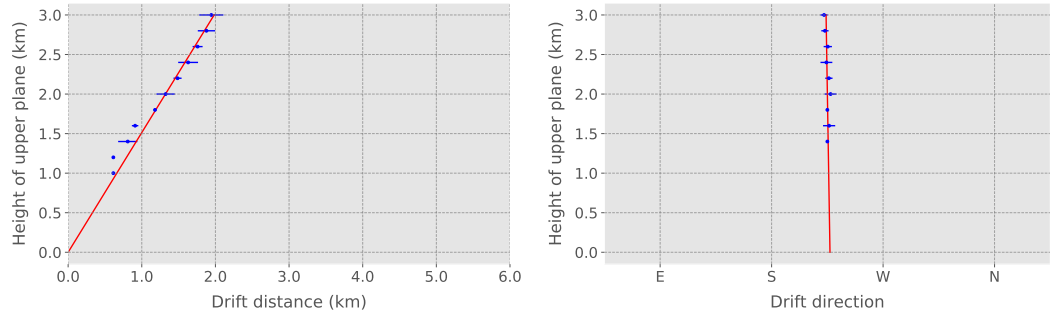
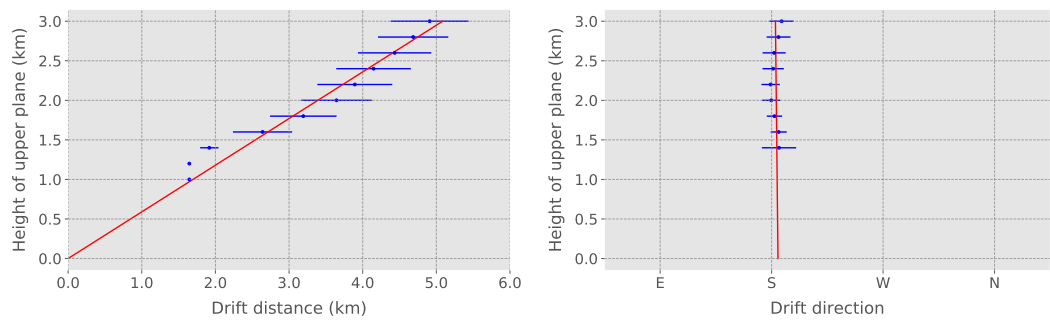


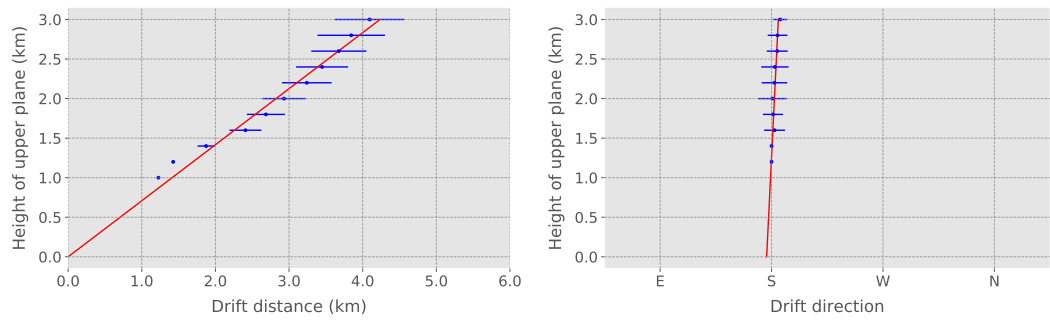
Figure A.3: Standard deviation for relative drift profiles from 30 minutes before to 30 minutes after the maximum of the precipitation events a) to c). Blue dots are the mean relative drift at that height, blue lines depict the standard deviation. On the left: Profile of relative drift distance. On the right: Profile of relative drift direction. A linear least-squared fit is visualized as the red line. An offset was added to all values of the distance-profile, so that the fitted drift distance at ground equals 0.



(d)



(e)



(f)

Figure A.4: Same as Figure A.3, but for the precipitation events d) to f).

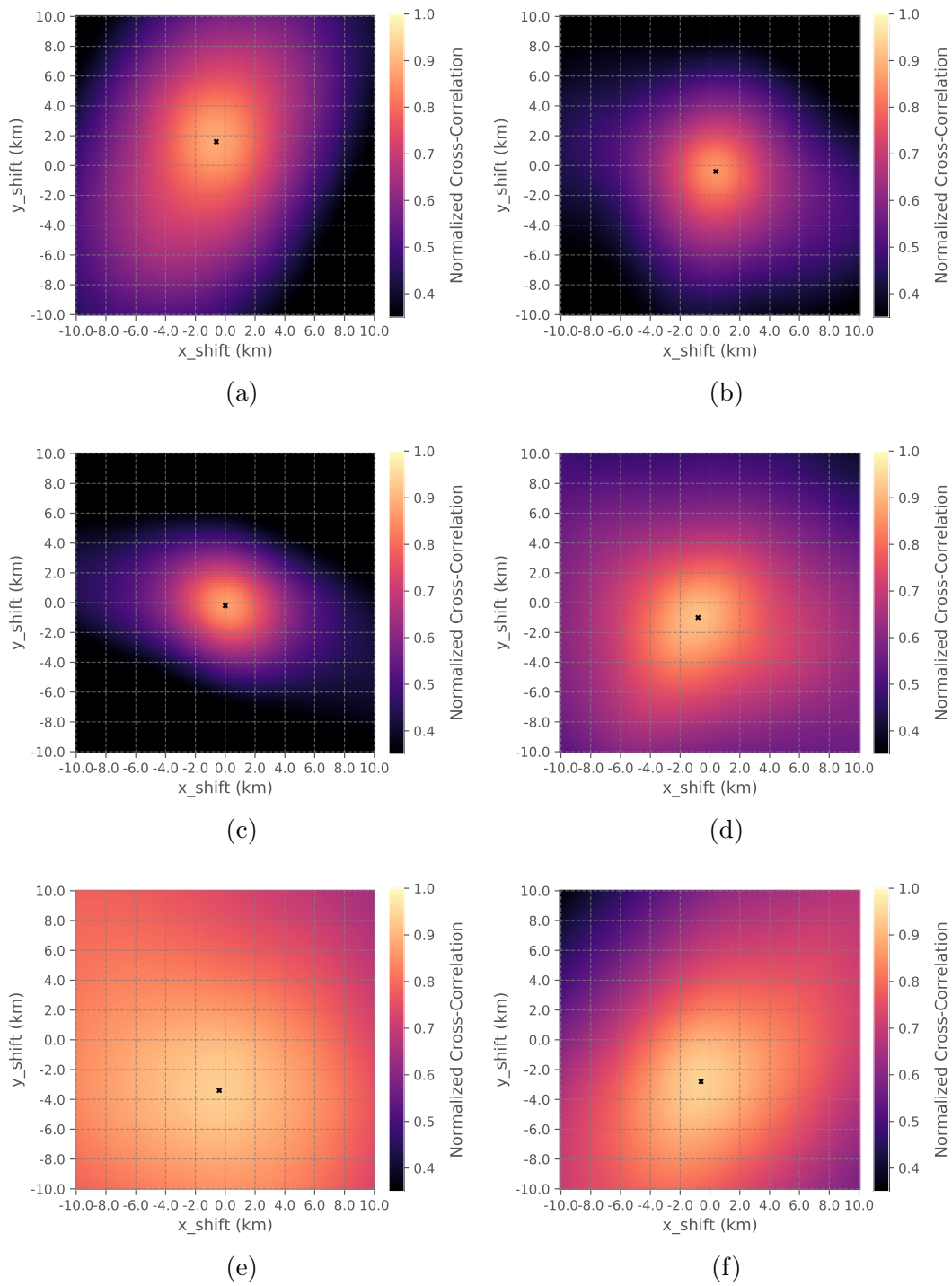


Figure A.5: Normalized Cross-Correlation matrix between the CAPPIs at 1 km and 3 km for the precipitation events a) to f).

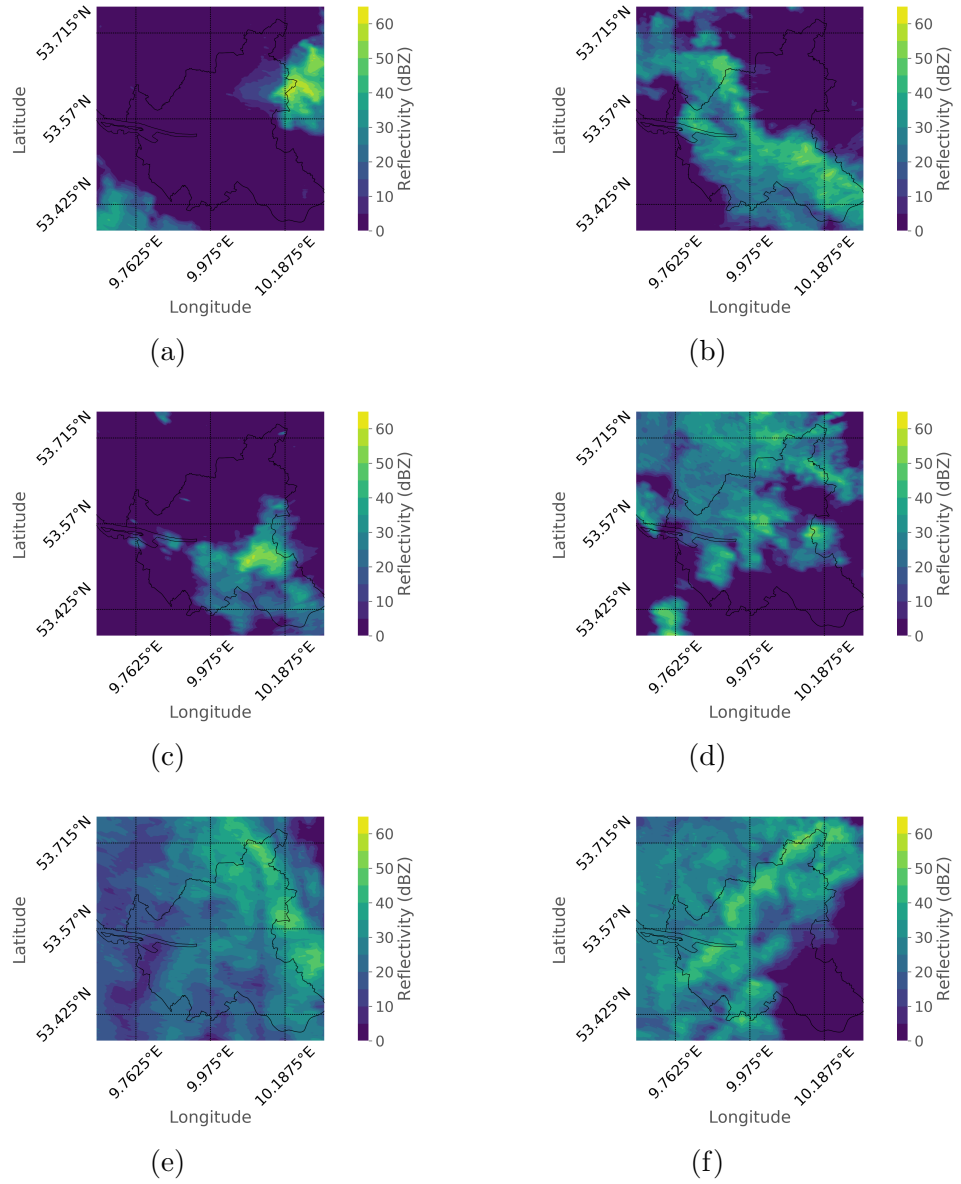


Figure A.6: With the PMA corrected precipitation scans over Hamburg for the precipitation events a) to f).

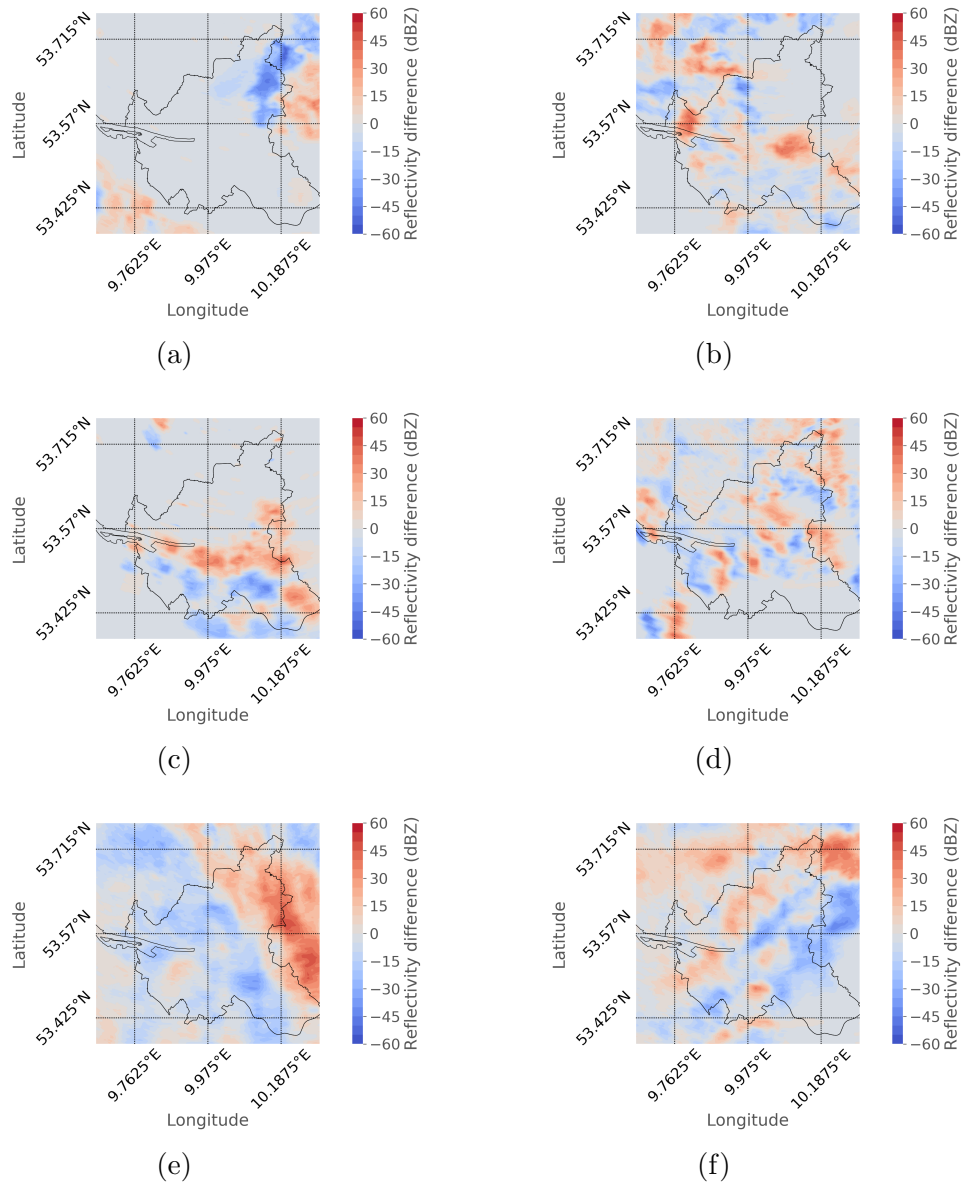


Figure A.7: Difference between corrected and original precipitation scans over Hamburg for the precipitation events a) to f).

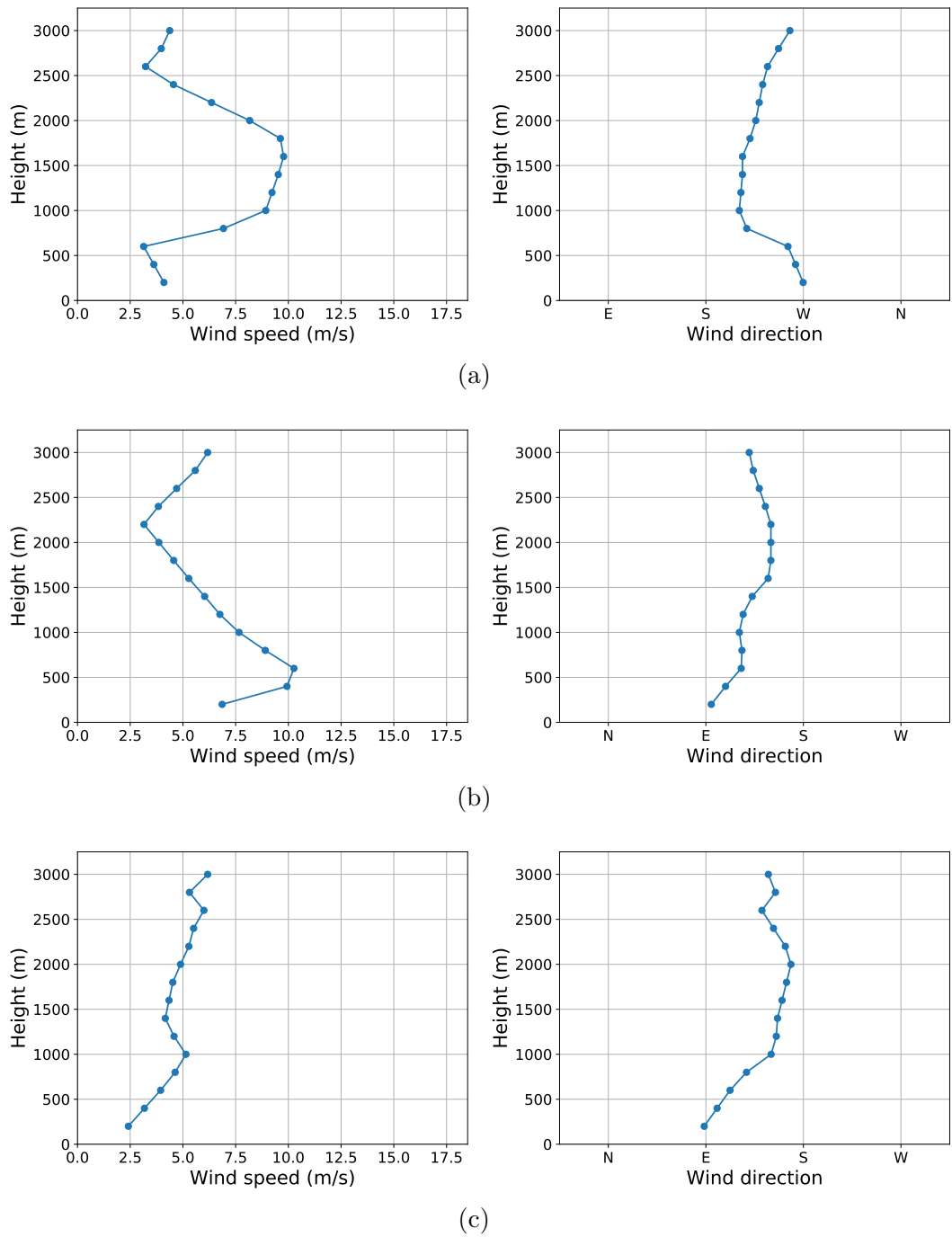
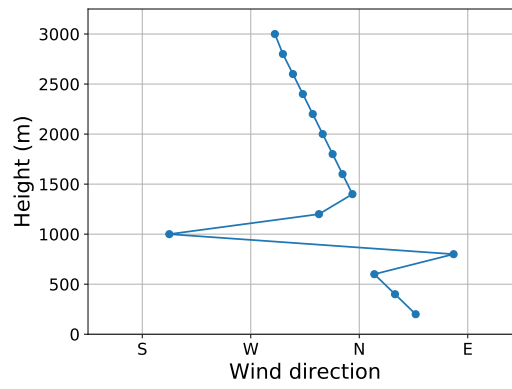
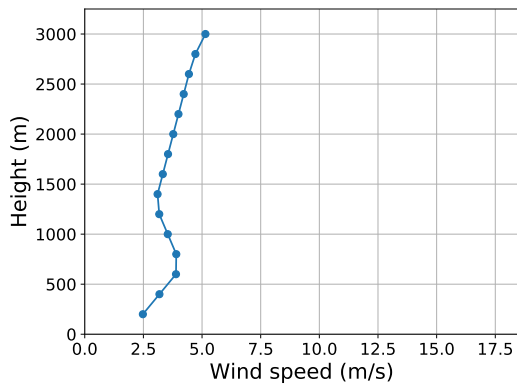
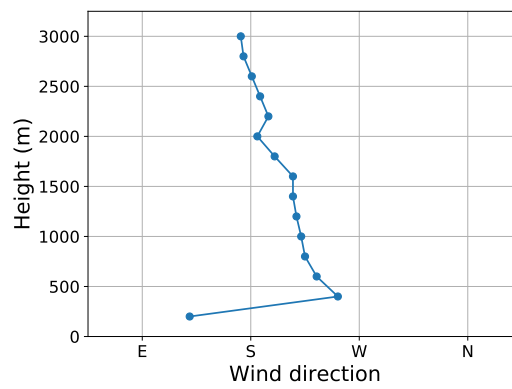
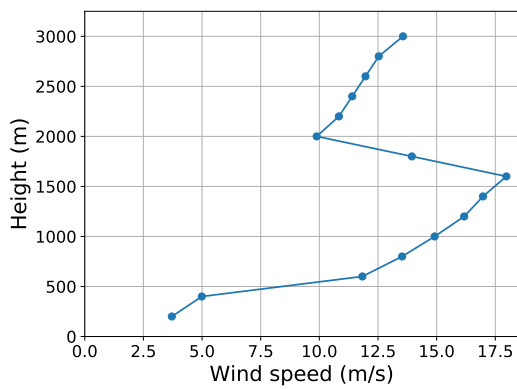


Figure A.8: Wind profiles measured by the Schleswig-sounding on a) 07.06.2016 12 UTC, b) 14.06.2016 00 UTC, c) 14.06.2016 12 UTC. Left side: Wind speed, right side: Wind direction.

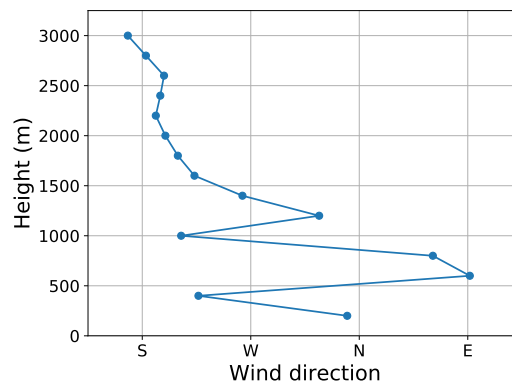
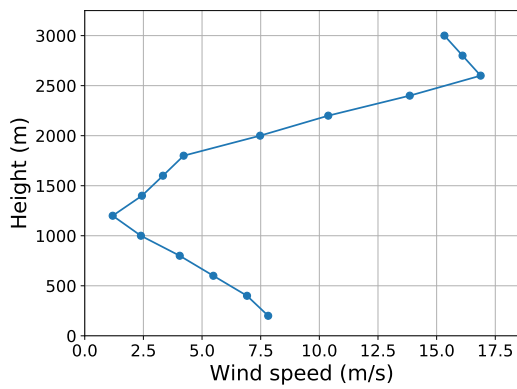
Appendix A. Plots for all Precipitation Events



(d)



(e)



(f)

Figure A.9: Same as Figure A.8, but for the precipitation events d) to f):
Sounding of d) at 17.06.2016 12 UTC, e) 24.06.2016 00 UTC,
f) 25.06.2016 12 UTC.

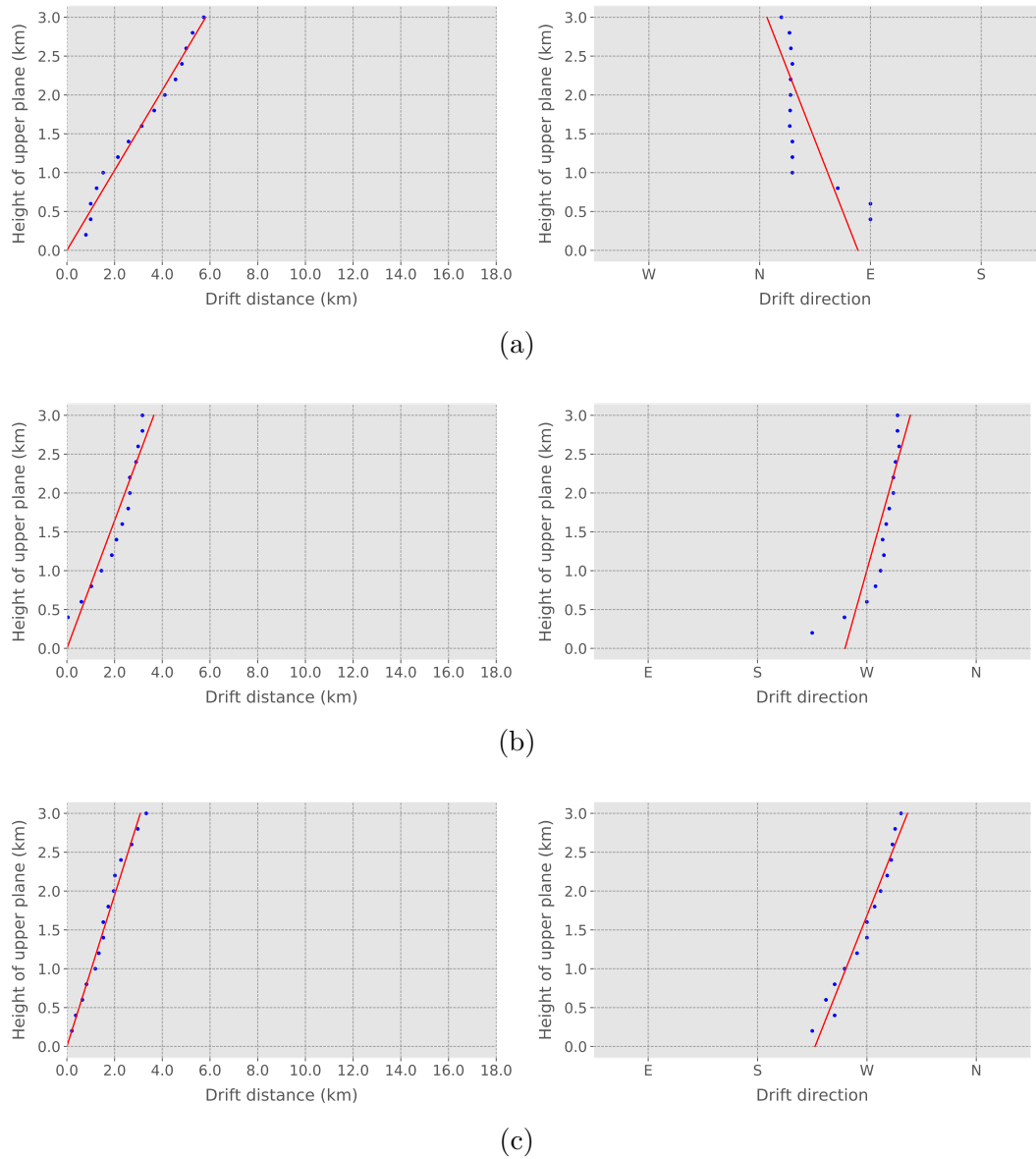
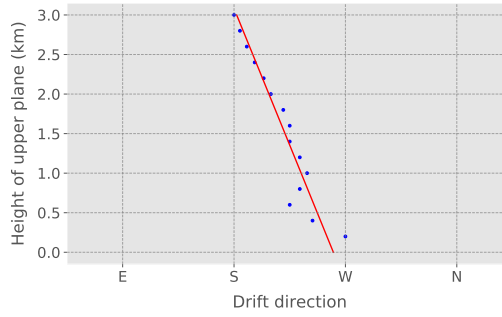
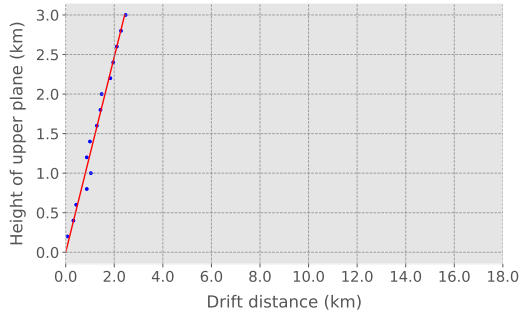
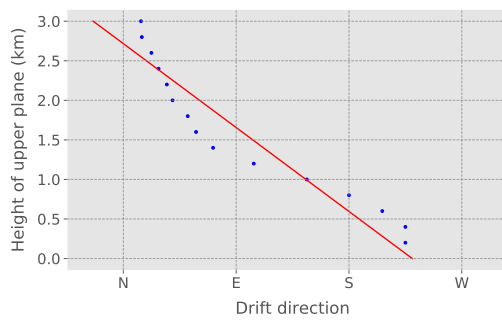
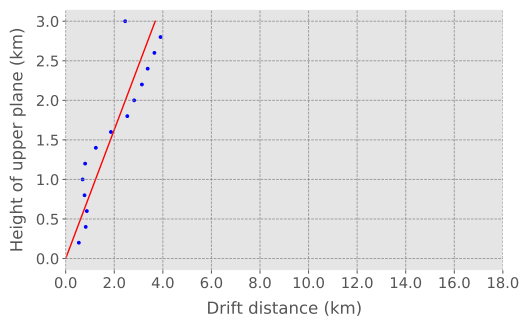


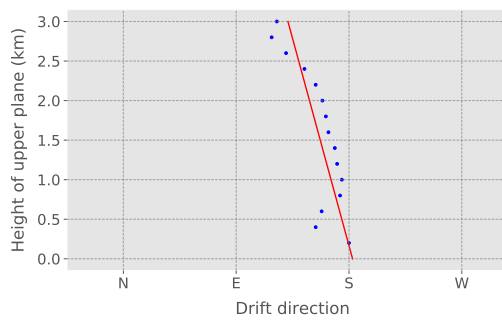
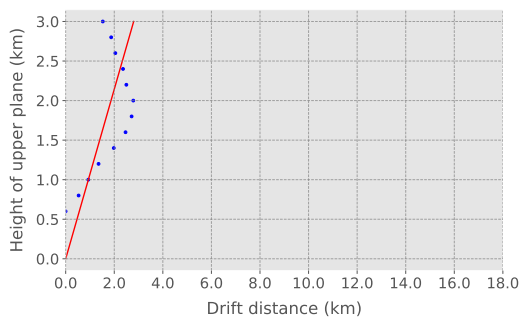
Figure A.10: Simulated relative drift profiles by the advection scheme. On the left-hand side: Profile of relative drift distance. On the right-hand side: Profile of relative drift direction. Blue dots are drift values as calculated by the template matching algorithm for the simulated reflectivity fields. A linear least-squared fit is visualized as the red line. An offset was added so that the wind drift distance of the linear fit at ground equals zero.



(d)



(e)



(f)

Figure A.11: Same as Figure A.10, but for the precipitation events d) to f).

Versicherung an Eides statt

Hiermit versichere ich an Eides statt, dass ich die vorliegende Arbeit im Studiengang M.Sc. Meteorologie selbstständig verfasst und keine anderen als die angegebenen Hilfsmittel – insbesondere keine im Quellenverzeichnis nicht benannten Internet-Quellen – benutzt habe. Alle Stellen, die wörtlich oder sinngemäß aus Veröffentlichungen entnommen wurden, sind als solche kenntlich gemacht. Ich versichere weiterhin, dass ich die Arbeit vorher nicht in einem anderen Prüfungsverfahren eingereicht habe und die eingereichte schriftliche Fassung der auf dem elektronischen Speichermedium entspricht.

Gregor Möller

Ort, Datum